CTP and *parS* control ParB partition complex dynamics and ParA-ATPase activation for ParABS-mediated DNA partitioning

Running title: CTP- and *parS*-controlled F-plasmid partition

Keywords: Plasmid partition, ParABS system, Chromosome segregation, CTPase

James A. Taylor[1,3], Yeonee Seol[2], Keir C. Neuman[2] and Kiyoshi Mizuuchi[1*]

[1] Laboratory of Molecular Biology, National Institute of Diabetes and Digestive and Kidney Diseases, National Institutes of Health

[2] Biochemistry and Biophysics Center, National Heart, Lung, and Blood Institute, National Institutes of Health

[3] current address: Nuffield Department of Medicine, University of Oxford

* Corresponding author: kiyoshimi@niddk.nih.gov

Abstract

ParABS partition systems, comprising the centromere-like DNA sequence *parS,* the *parS*-binding ParB-CTPase and the nucleoid-binding ParA-ATPase, ensure faithful segregation of bacterial chromosomes and low-copy-number plasmids. F-plasmid partition complexes containing $ParB_F$ and $parS_F$ move by generating and following a local concentration gradient of nucleoid-bound $ParA_F$. However, the process of $ParB_F$ activation of $ParA_F$-ATPase has not been defined. We studied CTP- and $parS_F$-stimulated $ParA_F$—$ParB_F$ complex assembly leading to $ParA_F$-ATPase activation. Activation of DNA-bound $ParA_F$-ATP dimers for ATP hydrolysis requires binding of two $ParB_F$ N-terminal domains. CTP or $parS_F$ enhances the ATPase rate without increasing $ParA_F$—$ParB_F$ assembly kinetics. Together, $parS_F$ and CTP accelerate $ParA_F$—$ParB_F$ assembly without further increasing the ATPase rate. Magnetic-tweezers experiments showed that CTP promotes multiple $ParB_F$ loading onto $parS_F$-containing DNA, generating condensed partition complex-like assemblies. We propose that $ParB_F$ in the partition complex adopts a conformation that enhances $ParB_F$—$ParB_F$ and $ParA_F$—$ParB_F$ interactions promoting efficient partitioning.

26 **Introduction**

27 Faithful segregation of replicated chromosomes is essential for efficient proliferation of cells.
28 Accordingly, many bacteria are equipped with active chromosome and plasmid partition systems
29 belonging to the ParABS family (Baxter and Funnell, 2014; Lutkenhaus, 2012; Vecchiarelli et al.,
30 2012). Basic ParABS systems comprise two proteins, ParA and ParB, and a centromere-like, cis-
31 acting DNA element called *parS*. The ParA proteins of this family are ATPases with a
32 characteristic deviant Walker-A motif (Motallebi-Veshareh et al., 1990) and bind non-specific
33 DNA (nsDNA) in an ATP-dependent manner by forming a DNA binding-competent dimer (Davey
34 and Funnell, 1994; Leonard et al., 2005; Vecchiarelli et al., 2010). Accordingly, ParA proteins
35 localize to the bacterial chromosome (the nucleoid) *in vivo* (Ebersbach and Gerdes, 2004; Hatano
36 et al., 2007; Lim et al., 2014).

37 ParB is typically a dimeric sequence-specific DNA binding protein that binds tightly to the *parS*
38 consensus sequences that mark the DNA cargo to be partitioned (Bouet et al., 2000; Mori et al.,
39 1989; Pillet et al., 2011; Taylor et al., 2015). Most ParABS systems have multiple copies of a ParB
40 dimer binding consensus sequence that collectively constitute a *parS* site. F-plasmid has a *parS*
41 sequence cluster ($parS_F$, also called *sopC*) composed of twelve repeats of a 16 bp consensus
42 sequence, each separated by fourteen base-pair spacer sequences (Helsberg and Eichenlaub, 1986).
43 The ParBs of known chromosomal and plasmid Par systems such as P1 and F bind to *parS via* a
44 helix-turn-helix motif (Schumacher and Funnell, 2005; Schumacher et al., 2010). These HTH-
45 ParB proteins also associate with several kilobases of DNA surrounding a *parS* site *in vivo* in a
46 proximity-dependent manner without obvious sequence specificity (Breier and Grossman, 2007;

Murray et al., 2006; Rodionov et al., 1999; Sanchez et al., 2015). This activity, known as ParB spreading, is believed to be essential for proper function of these systems (Breier and Grossman, 2007; Graham et al., 2014) and results in the formation of a large nucleo-protein complex (the partition complex) around the *parS* site on the DNA to be partitioned. Mutations in the *B. subtilis parB* gene blocking spreading and causing partition deficiency have been identified within the Box II region (GXRR) of the N-terminal domain (Breier and Grossman, 2007; Graham et al., 2014), a highly conserved motif among HTH-ParB homologues (Yamaichi and Niki, 2000). Recently, Soh and coworkers reported that HTH-ParB proteins have CTPase activity and the Box II residues play key roles in CTP binding and hydrolysis, indicating that ParB spreading is driven by an active process dependent on energy derived from CTP hydrolysis (Jalal et al., 2020; Soh et al., 2019).

ParB interacts with ParA *via* its N-terminal region (Ravin et al., 2003) and activates nsDNA-bound ParA dimer's ATPase, releasing it from DNA (Ah-Seng et al., 2009; Davis et al., 1992; Scholefield et al., 2011; Watanabe et al., 1992). In the absence of ParB stimulation, the ATP turnover of ParA is low, typically around one ATP per hour (Ah-Seng et al., 2009; Davis et al., 1992; Fung et al., 2001; Scholefield et al., 2011). Because of this slow basal ATPase rate, and since the majority of cellular ParB molecules is concentrated at the partition complexes due to ParB spreading, ATP hydrolysis by ParA and dissociation from the nucleoid is expected to occur principally in the vicinity of partition complexes. Biochemical studies of P1 ParA ATPase showed a significant time-delay before activation of ParA for DNA binding after ATP binding, predicting a significant free bulk-diffusion period for ParA before reactivation for nsDNA binding (Vecchiarelli et al., 2010). This, along with *in vivo* imaging observations (Hatano et al., 2007; Ringgaard et al., 2009), led to a prediction that the nucleoid proximal to a partition complex would become depleted of

69 ParA (the ParA depletion zone) and the proposal of a diffusion-ratchet model for plasmid
70 segregation by the ParABS system (Vecchiarelli et al., 2010).

71 The diffusion-ratchet model is based on the premise that the nucleoid-bound ParA-ATPase
72 activation by plasmid-bound ParB generates a local ParA depletion zone on the nucleoid, forming
73 a nucleoid-bound ParA concentration gradient around the partition complex (Hu et al., 2017;
74 Vecchiarelli et al., 2010). The interaction of plasmid-bound ParB with the ParA gradient on the
75 nucleoid results in a cargo position-dependent free-energy difference (Sugawara and Kaneko,
76 2011). Binding of ParB to ParA reduces the system free-energy, therefore moving the cargo to a
77 higher ParA concentration lowers the system free-energy. This cargo position-dependent free-
78 energy difference translates to a directional motive force on the ParB bound cargo. The generation
79 of sufficient cargo motive force to overcome thermal diffusion was established in cell-free
80 reconstitution experiments showing that a bead coated with $parS_F$-containing DNA is driven across
81 an nsDNA-coated flow cell surface in the presence of $ParA_F$, $ParB_F$ and ATP (Vecchiarelli et al.,
82 2014). In some *in vivo* time-lapse imaging experiments ParA has been observed to undergo pole-
83 to-pole oscillations along the length of a nucleoid with a partition complex chasing the receding
84 edge of a ParA distribution zone on the nucleoid, further supporting the diffusion-ratchet model
85 (Hatano et al., 2007; Ringgaard et al., 2009). Variations of this model have also been proposed (Le
86 Gall et al., 2016; Lim et al., 2014; McLeod et al., 2017).

87 Generating persistent directional motion by the diffusion-ratchet model requires a balance between
88 the ParA—ParB association/dissociation dynamics prior to ATP hydrolysis and the steps and
89 kinetic parameters that govern ATP hydrolysis. For example, if every ParA—ParB association

90 resulted in instantaneous ATP hydrolysis and dissolution of the ParA—ParB bonds linking the
91 partition complex (cargo) and the nucleoid, no cargo driving force would result. Conversely, if
92 each bond persisted too long the cargo would remain immobile on the nucleoid (Hu et al., 2017).
93 However, the detailed biochemical reaction steps leading to ParB activation of DNA-bound ParA-
94 ATPase and the subsequent release of ParA have not been determined.

95 In order to advance our quantitative understanding of the ParABS system mechanism, we
96 investigated the assembly and disassembly kinetics of $ParA_F$—$ParB_F$ complexes that form prior to
97 ATP hydrolysis using F-plasmid $ParA_FB_FS_F$ (also called SopA/B/C) as a model system. Employing
98 a TIRF microscopy-based nsDNA-carpet assay (Vecchiarelli et al., 2013) we first examined the
99 stoichiometry of the nsDNA-bound $ParA_F$—$ParB_F$ complexes that accumulate in the absence of
100 ATP hydrolysis by substituting ATP with non-hydrolysable ATPγS in the presence of different
101 $ParB_F$-cofactors (*parS* and CTP) or introducing $ParB_F$ mutants that hinder $ParB_F$ dimerization,
102 $parS_F$-binding, or $ParA_F$ ATPase activation. We then studied how the same set of cofactors or
103 $ParB_F$ mutations influenced $ParA_F$-ATPase activation by $ParB_F$. Our results showed that $ParB_F$
104 formed complexes with nsDNA-bound $ParA_F$ in which both $ParB_F$-interacting faces of the $ParA_F$
105 dimers were occupied by the N-terminal $ParA_F$-activation domain of $ParB_F$. All such complexes
106 observed in the presence of ATPγS exhibited similar, slow dissociation kinetics from nsDNA
107 compared to $ParA_F$ dimers in the absence of $ParB_F$ so long as both $ParB_F$-interacting faces of the
108 $ParA_F$ dimers were occupied by $ParB_F$ N-terminal domains. Binding of $ParB_F$ N-terminal domains
109 at both $ParB_F$-interaction faces is also necessary for efficient ATPase activation of nsDNA-bound
110 $ParA_F$ dimers. Strikingly, the $ParB_F$ cofactors, CTP and $parS_F$, acted synergistically to accelerate
111 the assembly of pre-ATP hydrolysis $ParB_F$—$ParA_F$ complexes on nsDNA. In line with this, a

112 magnetic tweezers-based DNA condensation assay revealed that stable DNA condensation by
113 $ParB_F$ required both CTP and *parS*$_{F,}$ suggesting that these cofactors promote both $ParA_F$—$ParB_F$
114 and $ParB_F$—$ParB_F$ interactions. This compaction of *parS*$_F$-containing DNA by $ParB_F$ in the
115 presence of CTP recapitulated the salient features of the condensed ParB spreading partition
116 complex observed *in vivo*, suggesting that $ParB_F$ in the presence of *parS*$_F$ and CTP closely reflects
117 the functional state of $ParB_F$ in the partition complexes *in vivo*. Interestingly, $ParB_F$ in these
118 conditions accelerated ATP turnover by the nsDNA-bound $ParA_F$ no more than two-fold compared
119 to $ParB_F$ without *parS*$_F$ and CTP, to a modest ~80 h^{-1}. These findings have important implications
120 for the diffusion-ratchet model of F-plasmid partition by the ParAB*S* system.

121

Figure 1. *Schematic of flow cell setup for visualizing the binding and dissociation of fluorescent proteins on DNA-carpet.*

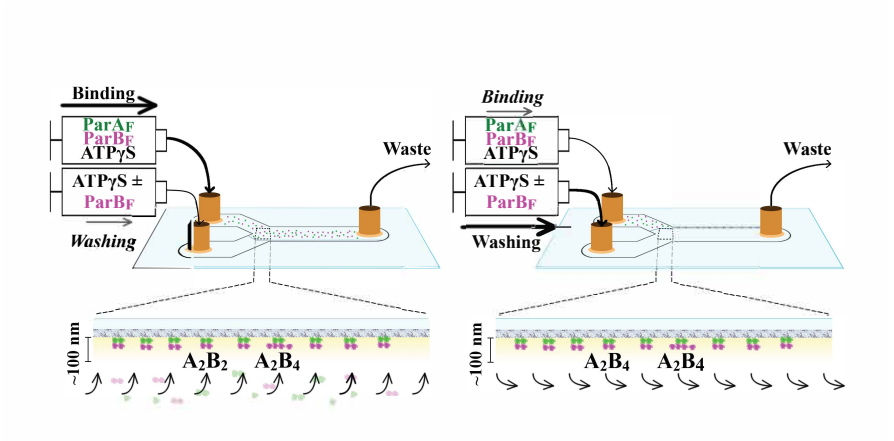

Figure 1. $ParA_F$-eGFP and $ParB_F$-Alexa647 proteins were flowed over a dense carpet of nsDNA attached to the supported lipid bilayer coated surface of a flow cell by biotin-streptavidin linkages. Imaging the surface of the flow cell by TIRF microscopy permits selective detection of the DNA-carpet bound proteins. Sample solution and the wash buffer, as specified for each experiment, were infused via two syringes at different infusion rates from separate inlets into a Y-shaped flow cell. A laminar boundary separates the two solutions downstream of the flow convergence point at the Y-junction. At the midpoint across the flow channel, downstream but close to the flow convergence point where the observations are made, the DNA-carpet area is exposed to the syringe content of the higher infusion rate. When the infusion rates of the two syringes are switched, the laminar boundary moves across the observation area and the solution flowing over the area switches. By switching the infusion rates of the two syringes repeatedly, multiple DNA-carpet-bound protein complex assembly and wash cycles can be recorded.

122

123 **Results**

124 Here, we investigated the ParA—ParB interactions that lead to accelerated ATP hydrolysis by
125 ParA and how they are impacted by *parS*$_F$ and CTP. First, we addressed the nature of nsDNA-
126 bound ParA$_F$—ParB$_F$ complexes. In the presence of ATP, ParA$_F$ forms DNA binding-competent
127 dimers and binds the nsDNA-carpet without ParB$_F$. Upon forming a complex with ParB$_F$, ParA$_F$
128 becomes activated for ATP hydrolysis and the complex rapidly disassembles (Vecchiarelli et al.,
129 2013), impeding characterization of the complex. Therefore, we studied DNA-bound ParA$_F$—
130 ParB$_F$ complexes that accumulate prior to ATP hydrolysis by using non-hydrolysable ATPγS. We
131 infused ParA$_F$-eGFP and ParB$_F$-Alexa647, or other fluorescent-labeled ParB$_F$ variants,
132 preincubated at room temperature for 10 min with ATPγS into an nsDNA-carpeted flow cell and
133 quantified the densities of the two DNA-associated proteins by imaging the flow cell surface with
134 TIRF microscopy (Figure 1). ParA$_F$ alone at the concentration used here (1 μM, all protein
135 concentrations are expressed as monomer concentrations) does not efficiently bind DNA in the
136 presence of ATPγS and low binding of ParA$_F$-eGFP was detected on the DNA-carpet (Figure 2A,
137 B). The observed DNA dissociation rate constant of ParA$_F$-ATPγS (~6 min^{-1}) is similar to that of
138 ParA$_F$-ATP estimated by FRAP, or by washing the flow-cell with nsDNA-containing buffer (~4.5
139 – 6 min^{-1}, Vecchiarelli, 2013). ParB$_F$-Alexa647 (2 μM) did not bind the DNA-carpet to a significant
140 level in the 300 mM K-glutamate buffer used in this experiment.

141 *The N-terminus of ParB$_F$ alone enhances DNA binding activity of ParA$_F$.*

142 We first examined if the N-terminal ParA$_F$-activation domain of ParB$_F$ (ParB$_F^{1-42}$) alone can induce
143 the ParA$_F$ conformational changes necessary for DNA binding in the presence of ATPγS. The

144 activation domain includes Arginine 36, which is critical for activation of $ParA_F$ ATPase (Ah-Seng
145 et al., 2009; Leonard et al., 2005), but lacks the CTPase- (AA63-155), *$parS_F$*-binding- (AA160-
146 272), and dimerization- (AA276-323) domains. For these experiments we used $ParB_F^{1-42}$ fused to
147 the N-terminus of mCherry ($ParB_F^{1-42}$-mCherry). This protein is a monomer in solution as judged
148 by its elution profile on a gel filtration column (Figure 1—figure supplement 1). $ParB_F^{1-42}$-mCherry
149 (10 μM) and $ParA_F$-eGFP (1 μM) bound the DNA-carpet together in the presence of ATPγS to a
150 density of ~5000 monomers/μm^2 maintaining ~1:1 stoichiometry (Figure 2C). When washed with
151 a buffer containing ATPγS, $ParB_F^{1-42}$-mCherry dissociated first, with an apparent dissociation rate
152 constant of ~5.7 min^{-1}, closely followed (within a few seconds) by $ParA_F$-eGFP dissociation
153 (Figure 2D). On the other hand, when the wash buffer contained 10 μM $ParB_F^{1-42}$-mCherry and
154 ATPγS, both proteins dissociated together, significantly slower than $ParA_F$-eGFP bound to the
155 DNA-carpet alone, with an apparent rate constant of ~0.9 min^{-1}, maintaining ~1:1 stoichiometry
156 (Figure 2E). FRAP measurements of $ParA_F$-eGFP—$ParB_F^{1-42}$-mCherry bound to the DNA-carpet
157 in the presence of ATPγS also indicated rapid exchange of $ParB_F^{1-42}$-mCherry (Figure 1—figure
158 supplement 2). Thus, at saturating $ParB_F^{1-42}$-mCherry concentration a $ParA_F$—ATPγS dimer is
159 bound by two molecules of $ParB_F^{1-42}$-mCherry occupying both sides of the $ParA_F$ dimer. The data
160 also indicate that $ParA_F$ dimers adopt a state of slowed dissociation from nsDNA when both of the
161 $ParB_F$-interacting faces are occupied by the $ParB_F$ N-terminal domain.

162 The nsDNA dissociation rate constants of $ParA_F$—$ParB_F$ complexes (including those involving
163 $ParB_F$ variants) and $ParB_F$:$ParA_F$ stoichiometry reported above and in the following sections are
164 summarized in Table 1.

165 Figure 2. *Monomeric $ParB_F^{1-42}$-mCherry can activate $ParA_F$ for nsDNA binding in the*

166 *presence of ATPγS by forming ~1:1 complex.*

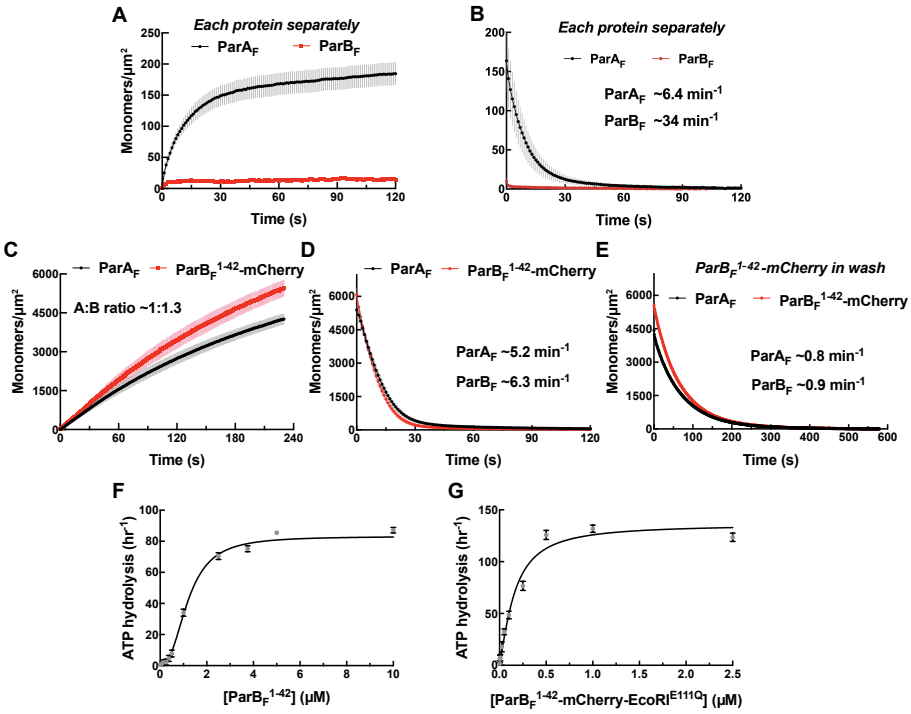

167

Figure 2. Protein sample solution in the presence of ATPγS (1 mM) was infused into nsDNA-carpeted flow cell at a constant flow to monitor the protein binding to the nsDNA, and the sample solution was switched to a wash buffer containing ATPγS to monitor protein dissociation from nsDNA. (A and B) Binding to, and dissociation from, nsDNA of $ParA_F$-eGFP (1 μM) or $ParB_F$-Alexa647 (2 μM) were measured separately. (C) $ParB_F^{1-42}$-mCherry (10 μM) and $ParA_F$-eGFP (1 μM) preincubated with ATPγS were infused into the nsDNA-carpeted flow cell and (D) washed with buffer containing ATPγS. (E) The washing experiment of D was repeated with washing buffer containing ATPγS and $ParB_F^{1-42}$-mCherry (10 μM). Time courses of above experiments and subsequent experiments of the same type in this study represent the average of several independent experiments

each comprising multiple repeated time-trajectory recordings. Error bars at each time point on the curve plots are SEM of all measurements. Dissociation rate constants (and the $ParB_F$:$ParA_F$ ratio where indicated) were calculated, unless otherwise noted, by first fitting individual time-trajectories with a single-exponential to obtain rate constants (or the B/A ratio of each carpet-bound protein density pair). The fit parameters were then averaged over repeated measurements within each experiment, and the mean and SEM for the set of experimental repeats were calculated. The calculated parameters shown in this figure, and other parameters calculated similarly, are summarized in Table 1. (F) $ParA_F$-ATPase activity (1 μM) was measured in the presence of EcoRI-digested pBR322 DNA (60 μg/ml) and different concentrations of $ParB_F^{1-42}$. (G) $ParA_F$-ATPase activity was measured as above in the presence of dimeric $ParB_F^{1-42}$-mCherry-$EcoRI^{E111Q}$. The ATPase stimulation curves in these and subsequent figures represent the average of three separate experiments unless otherwise specified (see Table 2), with error bars representing the SEM. Kinetic parameters were calculated as follows. $ParB_F$ dose-response curves, after subtraction of background without $ParA_F$, were fitted using a modified Hill equation: $v - v_0 = (v_{max} [B]^n) / (K_A^n + [B]^n)$, to account for the sigmoidal concentration dependence observed in some experiments. For [B] on the x-axis, total $ParB_F$ concentration was used instead of free $ParB_F$ concentration due to technical issues in estimating the free $ParB_F$ concentration. v_0 represents ATPase activity in the absence of $ParB_F$. Combined with relatively high $ParA_F$ concentration needed for the assay, the meanings of K_A and the cooperativity factor *n* here differ from those in the standard adaptation of the Hill equation. The mean and SEM of the parameters extracted from repeated experiments were calculated. The kinetic parameters and number of experimental repeats are summarized in Table 2.

168 *$ParA_F$ ATPase activation requires binding of two copies of $ParB_F$ N-terminal domain to the $ParA_F$*
169 *dimer.*

170 $ParB_F^{1-42}$ stimulated $ParA_F$-ATPase (1 μM) with a clear sigmoidal $ParB_F^{1-42}$ concentration
171 dependence and a half-maximum activation concentration of ~1.2 μM (Figure 2F; Table 2). Thus,

172 monomeric $ParB_F^{1-42}$ appears to activate $ParA_F$-ATPase when it binds on both sides of the DNA-
173 bound $ParA_F$ dimers. To test if the observed sigmoidal concentration dependence is due to the
174 monomeric nature of $ParB_F^{1-42}$, we prepared the N-terminal region of $ParB_F$ fused to mCherry and
175 the nuclease activity deficient $EcoRI^{E111Q}$, $ParB_F^{1-42}$-mCherry-$EcoRI^{E111Q}$. This construct, with
176 expected dimerization Kd < 10 pM (Liu et al., 1998), efficiently activated $ParA_F$-ATPase at least
177 to a similar maximum rate as $ParB_F^{1-42}$, but with a K_{half} of ~0.15 μM, ~8-fold lower than $ParB_F^{1-42}$,
178 and displayed no noticeable sigmoidal concentration dependence (Figure 2G). Possible binding of
179 the inactive EcoRI domain to DNA does not appear to influence the ATPase activation properties
180 of this construct; addition of EcoRI-binding DNA fragment in the reaction did not impact the
181 ATPase activation (Figure 1—figure supplement 3). Based on these results, we conclude that both
182 $ParB_F$-binding faces of a $ParA_F$ dimer must be occupied by $ParB_F$ N-termini for stimulation of its
183 ATPase activity.

184 *$ParB_F^{1-42\ R36A}$ forms a rapidly disassembling complex with $ParA_F$ on the DNA carpet.*

185 An R36A mutation was reported to significantly compromise $ParB_F$'s ability to activate $ParA_F$'s
186 ATPase (Ah-Seng et al., 2009). To test whether this mutation affected $ParB_F$'s ability to form a
187 complex with $ParA_F$ we repeated the experiments shown in Figure 2C-E using $ParB_F^{1-42\ R36A}$-
188 mCherry. $ParB_F^{1-42R36A}$-mCherry and $ParA_F$-eGFP bound with an approximately 1:1 stoichiometry,
189 similar to $ParB_F^{1-42}$-mCherry but reached a steady-state density on the DNA-carpet of less than
190 10% of the density observed with $ParB_F^{1-42}$-mCherry (Figure 3A). When washed with buffer
191 containing ATPγS, $ParB_F^{1-42\ R36A}$-mCherry disassociated first followed by $ParA_F$, similar to the
192 results obtained with $ParB_F^{1-42}$-mCherry but $ParB_F^{1-42\ R36A}$-mCherry dissociated ~10-fold faster,

193 followed by dissociation of $ParA_F$-eGFP within a few seconds (Figure 3B). When the wash buffer
194 also contained 10 μM $ParB_F^{1-42\ R36A}$-mCherry the two proteins dissociated in parallel maintaining
195 1:1 stoichiometry (Figure 3C). Together these observations indicate that $ParB_F^{R36A}$ interacts with
196 $ParA_F$, but with a much faster dissociation rate constant compared to wild-type $ParB_F$. $ParB_F^{1-42\ R36A}$
197 could activate $ParA_F$-ATPase with an increased half-saturation concentration of 108 μM,
198 approximately 100-fold higher than $ParB_F^{1-42}$ (Figure 3D). These results explain the puzzling report
199 that while the R36A mutation abrogated plasmid partitioning, it did not impede oscillation of $ParA_F$
200 on the nucleoid (Ah-Seng et al., 2013). At the interface between the $ParA_F$-bound nucleoid and
201 partition complexes containing many $ParB_F$ dimers, the local $ParB_F$ concentration is expected to
202 be sufficiently high for this mutant protein to be able to activate $ParA_F$-ATPase to support
203 oscillation of the nucleoid-bound $ParA_F$ distribution. However, the altered $ParA_F$—$ParB_F$
204 interaction dynamics prior to ATPase activation likely diminish the mechano-coupling efficiency
205 of the system that result in the observed partition defect.

206 Figure 3. *$ParB_F^{1\text{-}42\ R36A}$-mCherry dissociates faster from nsDNA-carpet-bound $ParA_F$-ATPγS*

207 *dimer, and $ParA_F$-ATPase activation requires higher $ParB_F^{1\text{-}42\ R36A}$ concentration.*

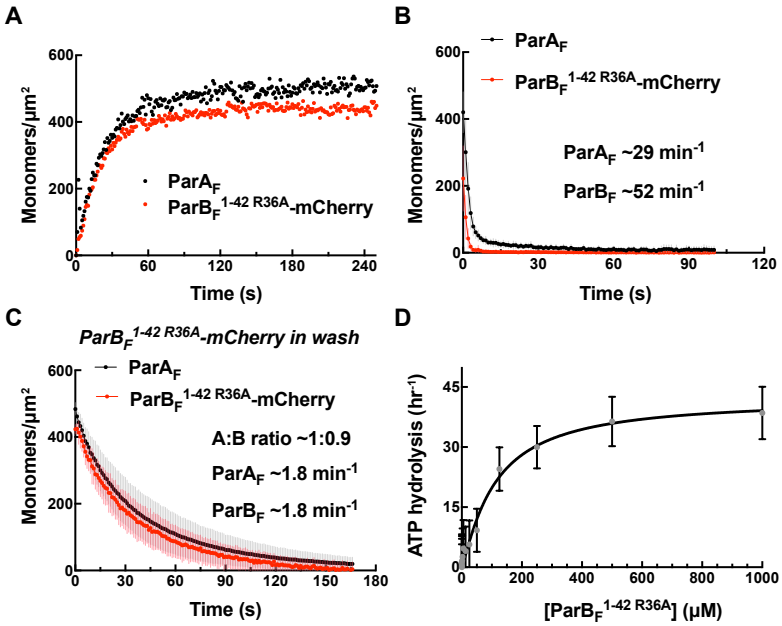

208

Figure 3. (A) $ParB_F^{1\text{-}42\ R36A}$-mCherry (10 μM) and $ParA_F$-eGFP (1 μM) preincubated with ATPγS were infused into the nsDNA-carpeted flow cell and then (B) washed with buffer containing ATPγS. (C) The washing experiment of B was repeated with buffer containing ATPγS and $ParB_F^{1\text{-}42\ R36A}$-mCherry (10 μM). (D) $ParA_F$-ATPase activity was measured in the presence of EcoRI-digested pBR322 DNA (60 μg/ml) as a function of $ParB_F^{1\text{-}42\ R36A}$ concentration. See Figure 2 legend and Tables 1 and 2 for additional details.

209

210 *$ParA_F$ and $ParB_F$ bind to and dissociate from nsDNA together in the presence of ATPγS with ~1:1*
211 *stoichiometry.*

212 When $ParA_F$-eGFP and full-length $ParB_F$-Alexa647 were incubated together at 1 μM and 2 μM,
213 respectively in the presence of ATPγS, they bound to the DNA-carpet in parallel maintaining ~1:1
214 stoichiometry up to a density of ~5000 monomers/μm^2 (Figure 4A). They also dissociated from
215 the DNA-carpet in parallel, maintaining ~1:1 stoichiometry, when washed with a buffer containing
216 ATPγS, with an apparent dissociation rate constant of approximately ~1 min^{-1} (Figure 4B). These
217 results show that $ParA_F$ and $ParB_F$ form a hetero-tetramer containing two monomers each of $ParA_F$
218 and $ParB_F$ (A_2B_2), or larger oligomers composed of the hetero-tetramers, that binds as a unit on
219 nsDNA in the presence of ATPγS.

220 Full size $ParB_F$, which forms dimer with apparent Kd of ~ 19 nM (Figure 4—figure supplement 1),
221 activated $ParA_F$-ATPase in the presence of nsDNA to ~50 hr^{-1} without significant sigmoidal
222 concentration dependence (Figure 4E). Based on the results of experiments with monomeric
223 $ParB_F^{1-42}$ proteins described earlier, we conclude that a single dimer of full-length $ParB_F$ can
224 straddle an nsDNA-bound $ParA_F$ dimer permitting the two N-termini to interact with both of the
225 $ParB_F$-binding faces of the $ParA_F$ dimer to activate the ATPase.

226 Figure 4. *$parS_F$ DNA alters protein stoichiometry of the $ParA_F$—$ParB_F$ complex formed prior*

227 *to ATP hydrolysis and the extent of $ParA_F$-ATPase activation by $ParB_F$.*

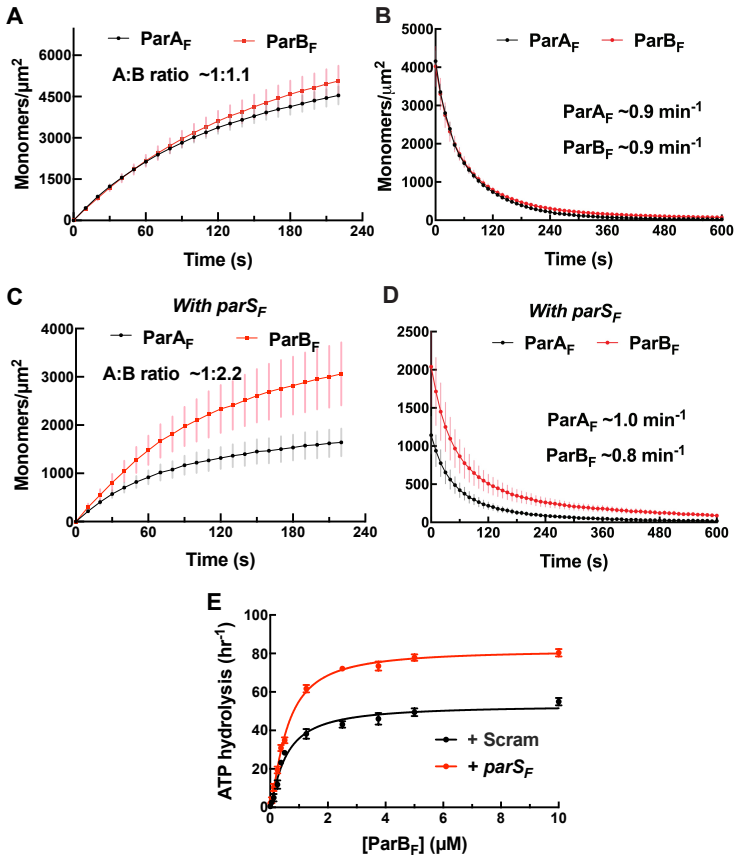

Figure 4. (A) $ParA_F$-eGFP (1 μM) and $ParB_F$-Alexa647 (2 μM) preincubated with ATPγS were infused into the nsDNA-carpeted flow cell and then (B) washed with buffer containing ATPγS. (C and D) As A and B except the sample included 24bp $parS_F$ DNA fragment (1.1 μM). (E) $ParA_F$-ATPase activity (1 μM) was measured in the presence of EcoRI-digested pBR322 DNA (60 μg/ml), different concentrations of $ParB_F$ and either a $parS_F$-DNA fragment or a DNA fragment with a scrambled sequence (1.1-fold higher concentrations than the $ParB_F$ dimers). See Figure 2 legend and Tables 1 and 2 for additional details.

228

229 *In the presence of $parS_F$, $ParB_F$ forms a 2:1 complex with $ParA_F$.*

230 We next asked if $ParB_F$ bound to $parS_F$ interacts differently with $ParA_F$ on the DNA-carpet. We
231 preincubated $ParA_F$-eGFP, $ParB_F$-Alexa647, ATPγS and a 24 bp duplex DNA fragment containing
232 a single $parS_F$ consensus sequence, at a slight molar excess over $ParB_F$ dimer, for 10 min at room
233 temperature. At the concentrations used, most of the $ParB_F$ dimers are expected to be bound to
234 $parS_F$. When infused into the DNA-carpeted flow cell, $ParA_F$-eGFP and $ParB_F$-Alexa647 bound to
235 and dissociated from the carpet with a stoichiometry of ~1:2 (Figure 4C, D), in sharp contrast to
236 the ~1:1 stoichiometry without $parS_F$ DNA. The kinetic parameters of the complex assembly and
237 disassembly were not significantly affected. These results demonstrate that $ParA_F$ and $ParB_F$ form
238 a complex of one $ParA_F$ dimer and two $ParB_F$ dimers (A_2B_4) in the presence of $parS_F$.

239 Does the change in protein stoichiometry caused by $parS_F$ translate to different levels of $ParA_F$-
240 ATPase activation? A previous study, comparing plasmid DNA with and without $parS_F$ as the
241 cofactor, showed that $ParB_F$ activates $ParA_F$-ATPase a few-fold more efficiently in the presence
242 of plasmid DNA containing a full $parS_F$ site (Ah-Seng et al., 2009). We titrated $ParB_F$ in the
243 presence of $ParA_F$, pBR322 DNA and 24 bp $parS_F$ duplex at a stoichiometric excess concentration
244 over the $ParB_F$ dimer. In the presence of $parS_F$ DNA, $ParB_F$ activated $ParA_F$-ATPase to a maximum
245 turnover rate of ~80 hr^{-1}, a ~60% increase compared to reactions where the $parS_F$ fragment was
246 replaced with a scrambled sequence fragment (Figure 4E). These results indicate that a single $parS_F$
247 DNA-bound $ParB_F$ dimer cannot straddle an nsDNA-bound $ParA_F$ dimer to activate the ATPase,

248 but by binding two $ParB_F$ dimers the ATPase activation level reaches slightly higher level than in
249 the absence of $parS_F$ DNA.

250 *Both CTP and CDP alter the complex formed between $ParA_F$ and $ParB_F$ in a manner similar to*
251 *$parS_F$, and CTP accelerates complex formation in the presence of $parS_F$.*

252 Since ParB proteins have recently been reported to have CTPase activity that is coupled to changes
253 in their DNA binding properties and ordering of their unstructured CTPase domains (Soh et al.,
254 2019), we next tested if the addition of CTP influences the $ParA_F$—$ParB_F$ complex formed on the
255 DNA-carpet in the presence of ATPγS. When $ParA_F$-eGFP and $ParB_F$-Alexa647 were incubated
256 together in the presence of ATPγS and CTP, they bound to and dissociated from the nsDNA-carpet
257 with a stoichiometry of ~1:2 (Figure 5A, Figure 5—figure supplement 1A). The assembly kinetics
258 of the carpet-bound complex was roughly the same as in the absence of CTP, however the apparent
259 dissociation rate constant during buffer wash was slightly but reproducibly slower by a factor of
260 roughly two at ~ 0.5 min^{-1}. The results were similar when CTP was replaced by CDP (Figure 5B,
261 Figure 5—figure supplement 1B). Inclusion of $parS_F$ DNA fragment in the reaction mixture
262 containing CDP did not dramatically change the results (Figure 5D, Figure 5—figure supplement
263 1D). However, when $parS_F$ was included together with CTP, the rate of A_2B_4 complex assembly
264 on the DNA-carpet increased several-fold, the binding density of the complex on the DNA-carpet
265 reached a correspondingly higher level, and the two proteins dissociated from the DNA-carpet
266 maintaining a ~1:2 stoichiometry with apparent dissociation rate constant similar to that in the
267 absence of $parS_F$ (Figures 5C, Figure 5—figure supplement 1C).

268 Next, we asked if the *parS*$_F$ DNA fragment was incorporated in the A_2B_4 complexes assembled in
269 its presence. The experiments in the presence of *parS*$_F$ were repeated in the presence or absence of
270 CTP with ParA$_F$ (1 μM), ParB$_F$-Alexa647 (2 μM) and Alexa488-*parS*$_F$ (1.1 μM), and the nsDNA-
271 carpet-bound ratio of *parS*$_F$ and ParB$_F$ after 240 sec sample infusion was measured (Figure 5E).
272 The observed *parS*$_F$ / (ParB$_F$)$_2$ ratio in the absence of CTP was ~0.2, while in the presence of CTP,
273 the ratio was only ~0.04. Thus, whereas the assembly of the A_2B_4 complex involving CTP-ParB$_F$
274 is accelerated by *parS*$_F$, a very small fraction of the resulting complex contained the *parS*$_F$-DNA
275 fragment, indicating that *parS*$_F$ plays a catalytic role in the assembly of the A_2B_4 complex.

276 *ParB*$_F$ *activates ParA*$_F$*-ATPase to the full extent without parS*$_F$ *in the presence of CTP*.

277 The maximum ParB$_F$ activation of ParA$_F$-ATPase in the presence of CTP, with or without *parS*$_F$,
278 was comparable to that of *parS*$_F$-bound ParB$_F$ in the absence of CTP (Figure 5F, G). The half-
279 saturation concentration of ParB$_F$ in the presence of *parS*$_F$ and CTP was significantly lower than
280 in the absence of CTP (~0.24 μM *vs* ~0.6 μM). Combined with the observation of faster assembly
281 of the complex on the DNA-carpet, a likely possibility is that in the presence of CTP and *parS*$_F$,
282 the ParB$_F$ dimer adopts a unique state that interacts with ParA$_F$ dimers with a higher association
283 rate constant.

284 Figure 5. *CTP and $parS_F$ together alter the interactions between the $ParB_F$ and $ParA_F$ dimers.*

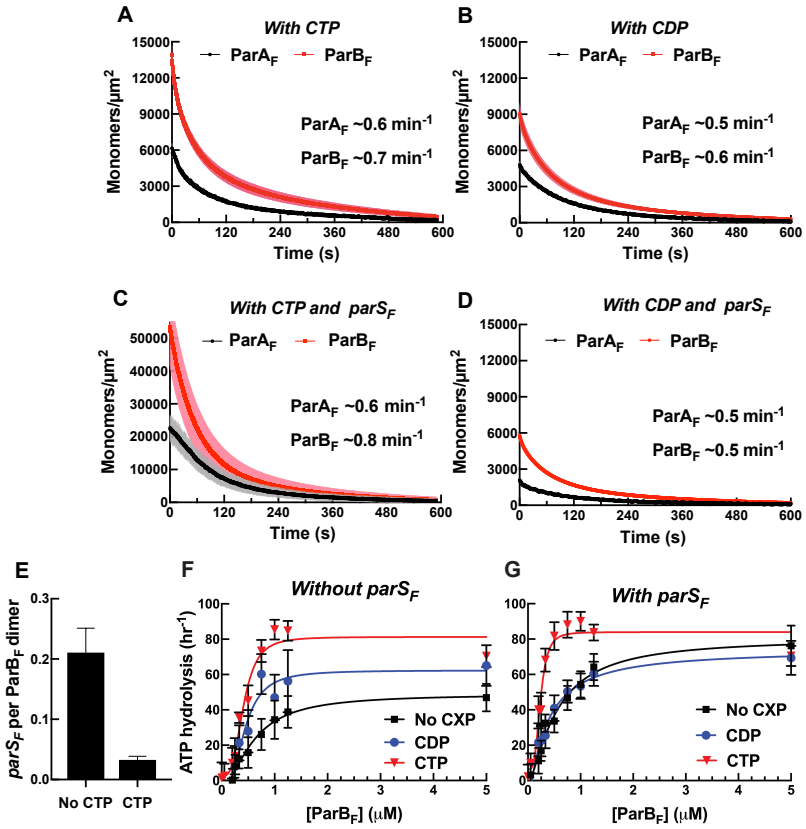

Figure 5. (A) $ParA_F$-eGFP (1 μM) and $ParB_F$-Alexa647 (2 μM) preincubated with ATPγS and CTP (2mM) were infused into the nsDNA-carpeted flow cell and then washed with buffer containing ATPγS and CTP. (B) As in A except CTP was replaced by CDP. (C) As in A, except 24 bp $parS_F$ fragment (1.1 μM) was added to the sample mixture. (D) As in B, except 24 bp $parS_F$ fragment (1.1 μM) was added to the sample mixture. For binding curves, see Figure 5—figure supplement 1A-D. (E) $ParA_F$ (1 μM), $ParB_F$-Alexa647 (2 μM) and Alexa488-labeled 24 bp $parS_F$ fragment (1.1 μM) preincubated with ATPγS or ATPγS plus CTP (2mM) were infused into the nsDNA-carpeted flow cell and after 240 sec, the ratio of the carpet-bound $parS_F$ fragment and $ParB_F$ dimer was measured. (F) $ParA_F$-ATPase activity was measured in the presence of EcoRI-digested

pBR322 DNA (60 μg/ml), different concentrations of $ParB_F$ and either no C-nucleotide, 2mM CDP or 2mM CTP. (G) As in F except the reactions also contained 24 bp $parS_F$ fragment (1.1-fold higher concentrations than $ParB_F$ dimers). See Figure 2 legend and Tables 1 and 2 for additional details.

285

Table 1. Apparent disassembly or exchange rate constants (min^{-1}) and $ParB_F/ParA_F$ ratio from fits of TIRFM wash and FRAP experiments.

Table 1: Apparent disassembly or exchange rate constants (min^{-1}) and $ParB_F/ParA_F$ ratio from fits of TIRFM wash and FRAP experiments.

	$ParA_F$	**$ParA_F$ + $ParB_F^{1-42}$**		**$ParA_F$ + $ParB_F^{1-42\ R36A}$**		**FRAP**		**$ParA_F$ + $ParB_F$**		**$ParA_F$ + $ParB_F$ + CDP**		**$ParA_F$ + $ParB_F$ + CTP**		**$ParA_F$ + $ParB_F^{R121A}$**	
Protein Measured	***$ParA_F$***	***$ParA_F$***	***$ParB_F$***	***$ParA_F$***	***$ParB_F^{1-42\ R36A}$***	***$ParA_F$***	***$ParB_F^{1-42}$***	***$ParA_F$***	***$ParB_F$***	***$ParA_F$***	***$ParB_F$***	***$ParA_F$***	***$ParB_F$***	***$ParA_F$***	***$ParB_F^{R121A}$***
- $parS_F$	**6.4± 0.6 N=4 (12)**	**5.2± 0.2 N=2 (9)**	**6.3± 0.3 N=2 (9)**	**29± 2 N=3 (9)**	**52± 4 N=3 (9)**	**2.0± 0.08 N=3 (11)**	**15.3± 2.1** N=3 (12)**	**0.93± 0.07 N=2 (6)**	**0.89± 0.09 N=2 (6)**	**0.53± 0.02 N=3 (11)**	**0.59± 0.03 N=2 (12)**	**0.63± 0.04 N=2 (7)**	**0.65± 0.10 N=2(7)**	**0.89± 0.01 N=3 (8)**	**0.78± 0.05 N=3 (8)**
		1 : 1.27± 0.06 N=2 (8)		*1 : 0.92± 0.02*** N=3 (9)*				*1 : 1.10± 0.13 N=3 (9)*		*1 : 1.49± 0.04 N=2 (7)*		*1 : 2.16± 0.15 N=3 (10)*		*1 : 0.99± 0.01 N=3 (8)*	
+ $parS_F$	*N.D.*	*N.D.*		*N.D.*		*N.D.*		***0.95± 0.04* N=2 (6)**	***0.82± 0.01* N=2 (6)**	**0.46± 0.02 N=2 (7)**	**0.53± 0.01 N=2 (7)**	**0.60± 0.08 N=2 (5)**	**0.83± 0.12 N=2 (6)**	**0.91± 0.01 N=3 (8)**	**0.78± 0.04 N=3 (8)**
								1 : 2.17± 0.40 N=3 (9)		*1 : 2.53± 0.07 N=2 (6)*		*1 : 2.16± 0.27 N=2(6)*		*1 : 1.12± 0.01 N=3 (12)*	
$ParB_F^{1-42}$ or $ParB_F^{1-42\ R36A}$ in wash	*N.D.*	**0.84± 0.01* N=1 (3)**	**0.89± 0.02* N=1 (3)**	**1.8± 0.4 N=3 (9)**	**1.8± 0.4 N=3 (9)**	*N.D.*		*N.D.*		*N.D.*		*N.D.*		*N.D.*	

The apparent dissociation (or FRAP) rate constants were obtained for individual time-trajectories by single-exponential curve fitting (except ** where the rate of faster decay, (68 +/- 0.5%) of a double-exponential fitting is shown), averaged for repeats within an experiment, and the mean and SEM for the set of independent experiments are shown in **bold characters** (except *where standard deviation among non-independent repeats within an experiment is shown). (N is the number of separate experiments, with total number of binding/wash cycles for repeated data collection in parenthesis.) ParA:ParB ratios were calculated from the final phase of the individual association time-trajectories (except *** where it was based on the beginning part of the washing phase in the presence of $ParB_F^{1-42\ R36A}$), averaged for the repeats within an experiment, and the mean and SEM for the set of independent experiments are shown in *non-bold italicized characters*. N.D., not done.

Table 2. ATPase kinetic parameters.

	$ParB_F$		**$ParB_F$ CTP**		**$ParB_F$ CDP**		**$ParB_F^{R121A}$**		**$ParB_F^{1-42}$**	**$ParB_F^{1-42\ R36A}$**	**$ParB_F^{1-42}$-mCherry-$EcoRI^{E111Q}$**	
	Scram N = 6	*$parS_F$* N = 6	*Scram* N = 3	*$parS_F$* N = 3	*Scram* N = 3	*$parS_F$* N = 3	*Scram* N = 3	*$parS_F$* N = 3	N = 6	N = 3	*Scram* N = 3	*EcoRI DNA* N = 2
v_{max} (hr^{-1})	54 *± 4.6*	79 *± 2.0*	79 *± 8.1*	78 *± 7.6*	71 *± 8.5*	87 *± 5.3*	60 *± 4.8*	62 *± 5.3*	83 *± 3*	38 *± 2*	131 *± 13*	125 *± 9*
K_A (µM)	0.53 *± 0.09*	0.59 *± 0.03*	0.41 *± 0.05*	0.24 *± 0.02*	0.42 *± 0.06*	0.34 *± 0.04*	0.86 *± 0.11*	1.1 *± 0.1*	1.2 *± 0.1*	108 *± 13*	0.16 *± 0.04*	0.16 *± 0.03*
Cooperativity coefficient (n)	1.2 *± 0.2*	1.4 *± 0.1*	3.3 *± 1.0*	3.6 *± 1.5*	2.6 *± 0.8*	1.1 *± 0.1*	2.5 *± 0.6*	1.6 *± 0.3*	2.5 *± 0.3*	1.5 *± 0.2*	1.4 *± 0.3*	1.4 *± 0.2*

ATPase measurements were performed with $ParA_F$ (1 µM) and different mutants of $ParB_F$, 60 µg/ml EcoRI-digested pBR322 DNA plus Scram- or *$parS_F$*-DNA fragment and CTP or CDP, as indicated in the column headings.
Assays were repeated "N" times, each data set of an assay were fit to a modified Hill equation as specified in the legend for Figure 2, and the mean and standard error of the mean (SEM) for the N measurements are shown. v_{max} is the maximum stimulated ATPase turnover number of $ParA_F$, K_A is the apparent total concentration of $ParB_F$ necessary for half maximum stimulation and **n** is the apparent cooperativity coefficient.

286 *In the presence of CTP $ParB_F$ condenses DNA carrying $parS_F$ in cis.*

287 A recent study showed that *B. subtilis* chromosomal ParB binds CTP *via* the highly conserved Box
288 II motif, which in turn triggers a conformational change in the N-terminal proximal regions in a
289 *parS* dependent manner (Soh et al., 2019). This CTP-*parS* dependent ParB conformational change
290 appears to promote ParB DNA binding and spreading (Soh et al., 2019), impacting ParB-DNA

291 partition complex assembly. *In vivo*, spreading ParB forms condensed foci around *parS* sites
292 indicating that *parS* driven ParB spreading likely occurs *in cis*. Nonetheless, the possibility that
293 *parS* can trigger ParB spreading *in trans* has not been tested *in vitro*. Previous studies have reported
294 DNA condensation by *B. subtilis* ParB via ParB—ParB interactions, but these studies were
295 conducted in the absence of CTP and did not see a strong effect of *parS in cis* (Graham et al., 2014;
296 Song et al., 2017; Taylor et al., 2015). To see if $parS_F$ can act *in-trans* and to characterize how
297 $parS_F$ and CTP influence $ParB_F$—DNA interactions *in vitro*, we conducted single-molecule DNA
298 pulling experiments employing magnetic tweezers. $ParB_F$ at various concentrations was infused
299 into a flow cell containing ~ 5 kbp DNA tethers that were immobilized on the coverslip surface at
300 one end and attached to a magnetic bead on the other (Figure 6A). The tethers contained either
301 twelve $parS_F$ consensus sequence repeats of F-plasmid at their midpoints ($parS_F$-DNA), or no
302 $parS_F$ sequence (nsDNA). The protein sample was infused while the DNA tethers were stretched
303 at 5 pN force preventing DNA condensation. To allow DNA condensation by tether-bound inter-
304 $ParB_F$ dimer bridges, the force was dropped to 0.05 pN and the DNA tether extension was
305 monitored for 30 sec. To assess the stability of DNA condensation by $ParB_F$ dimers, tether
306 extension was monitored after increasing the force to 5 pN. The degree of condensation was
307 expressed as the decrease in magnetic bead height relative to the height prior to introduction of
308 $ParB_F$ (average extension measured over 5 sec immediately following force application). In the
309 absence of CTP, we only observed condensation at very high concentrations of $ParB_F$ (>5 μM) and
310 did not see a significant difference between $parS_F$-containing and non-specific tethers (Figure 6B
311 inset). However, in the presence of CTP, 50 nM $ParB_F$ robustly condensed $parS_F$-containing DNA
312 tethers (Figure 6B). These condensed protein-DNA complexes resisted 5 pN extension force,

313 requiring many minutes at 5 pN tension to de-condense (Figure 6—figure supplement 1A). The
314 slow de-condensation took place through a series of abrupt steps, which we interpret as stepwise
315 opening of large DNA loops held by multiple $ParB_F$—$ParB_F$ interactions (Figure 6—figure
316 supplement 1A). We observed some condensation events with $parS_F$ containing tethers in the
317 presence of CDP, but these events were rarer, required higher $ParB_F$ concentrations, and were
318 almost completely de-condensed within 5 sec of raising the force to 5 pN, in stark contrast to
319 condensation in the presence of CTP (Figure 6B, Figure 5—figure supplement 1B). In contrast,
320 $ParB_F$ was unable to substantially condense DNA tethers lacking $parS_F$ sequences, even in the
321 presence of CTP, and rare condensation events were quickly reversed by the application of 5 pN
322 force (Figure 6B). Addition of $parS_F$-containing DNA fragments together with $ParB_F$ and CTP did
323 not rescue the inability to condense tethers lacking $parS_F$, indicating that $parS_F$ cannot act *in trans*
324 to promote ParB spreading and condensation of DNA molecules (Figure 6—figure supplement 2).
325 Together these results indicate that $parS_F$ mediates loading of multiple CTP-bound $ParB_F$ dimers
326 *in cis* onto the DNA-tethers and these $ParB_F$ dimers are capable of forming DNA looping bridges
327 likely *via* inter-dimer interactions to form a condensed partition complex-like structure. As
328 expected, $ParB_F^{R121A}$ bearing a mutation at the critical Box II residue in the CTPase domain was
329 unable to condense DNA to a significant degree even with $parS_F$ containing tethers (Figure 6B).
330 We propose that stable DNA condensation by $ParB_F$ is mediated by CTPase domain dimerization
331 and requires both $parS_F$ and CTP at moderate $ParB_F$ concentrations (~100 nM) (Figure 6C).

Even in the absence of CTP or CDP, $ParB_F^{R121A}$/ $ParA_F$ complexes neither exhibited a change of stoichiometry when assembled in the presence of ATPγS, nor a change in ATP turnover in response $parS_F$ observed with wild type $ParB_F$ (Figure 4), suggesting a connection between

$ParB_F$—$parS_F$ binding and the $ParB_F$ conformational change induced by C-nucleotide binding (Figure 6—figure supplement 3).

Figure 6. *Magnetic tweezers measurements of $parS_F$ and CTP-dependent DNA condensation by $ParB_F$.*

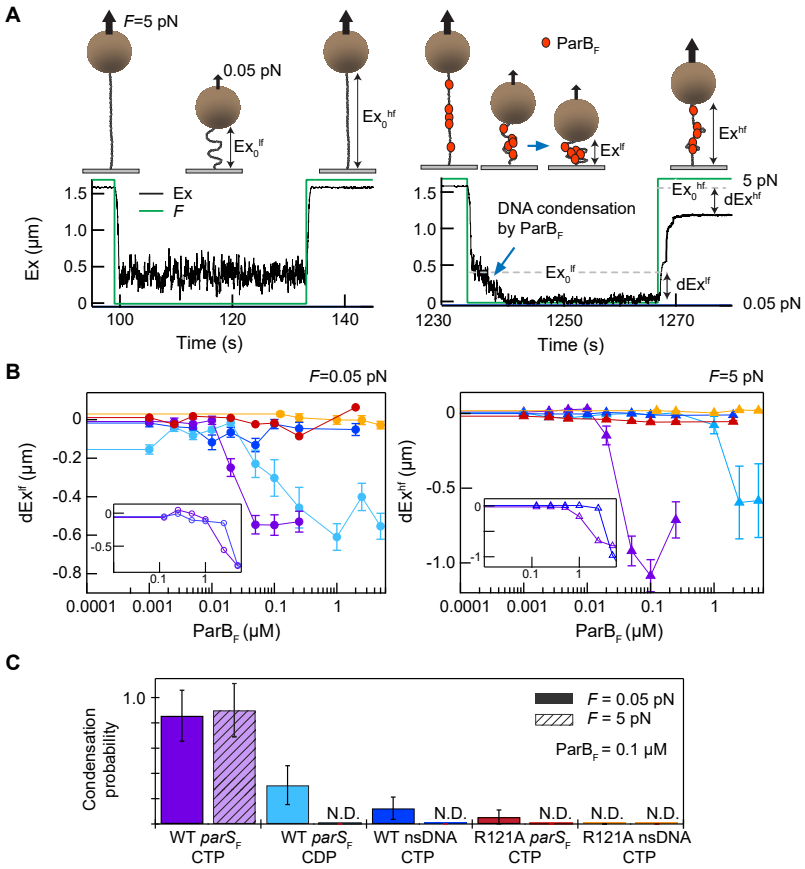

Figure 6. (A) Schematic showing the magnetic tweezers DNA condensation assay. One end of a 5 kb DNA molecule is attached to the surface of a flow-cell and the free end is attached to a 1 μm magnetic bead (brown sphere). The DNA extension (Ex) was measured by tracking the bead height from the surface at two different forces; 0.05 pN (low force, lf), and 5 pN (high force, hf). The extent of DNA condensation was estimated by obtaining the difference in DNA extension with and without $ParB_F$ under high and low force conditions. (B) Changes in extension at low force ($dEx^{lf} = Ex^{lf} - Ex_0^{lf}$), left panel, and at high force ($dEx^{hf} = Ex^{hf} - Ex_0^{hf}$), right panel, for 7 different conditions plotted as a function of $ParB_F$ concentration. Error bars represent

standard error of means (SEM). Negative dEx^{lf} indicates DNA condensation by tether-bound $ParB_F$ dimers whereas negative dEx^{hf} indicates DNA condensation resisting the high (5 pN) pulling force, indicating stable $ParB_F$-$ParB_F$ DNA-looping interactions. The reported DNA extensions were the averages of the last 5 seconds of the extension at low force (0.05 pN; circles) and the first 5 seconds of the extension at high force (5 pN; triangles). Different conditions are color coded as follows. Purple: $parS_F$-DNA tether with WT $ParB_F$ and CTP; light blue: $parS_F$-DNA tether with WT $ParB_F$ and CDP; dark blue: nsDNA tether with WT $ParB_F$ and CDP; red: $parS_F$-DNA tether with $ParB_F^{R121A}$ and CTP; orange: nsDNA tether with $ParB_F^{R121A}$ and CTP. For comparison with condensation in the presence of CTP, dEx data of $parS_F$-DNA tether and nsDNA tether with WT $ParB_F$ without CTP are displayed (inset, purple and blue open circles for 0.05 pN, purple and blue triangle for 5 pN respectively). (C) The condensation probabilities at 0.1 μM $ParB_F$ for 5 different conditions at 0.05 pN and 5 pN. The condensation probability was calculated by dividing the number of DNA tethers that exhibited DNA condensation by the total number of DNA tethers for each measurement condition. Except for $parS_F$-DNA with WT $ParB_F$ and CTP, all conditions show either minimal or negligible condensation probabilities. The different conditions are color-coded as indicated in B and the diagonal pattern indicates probabilities at 5 pN. Error bars represent standard error of means (SEM).

332 **Discussion**

333 In this report, we characterized facets of the $ParA_F$—$ParB_F$ interaction leading to the assembly of
334 the nsDNA-bound $ParA_F$—$ParB_F$ complex that is required to activate $ParA_F$ for ATP hydrolysis
335 and dissociation from nsDNA under the influences of *parS*$_F$ and CTP (Summarized in Figure 7).
336 Our results indicate that both $ParB_F$ binding faces of the nsDNA-bound $ParA_F$ dimers must be
337 occupied by a $ParB_F$ N-terminal domain for ATPase activation (Figure 2C-G and 7B). In principle,
338 two copies of the $ParB_F$ N-terminal domain activating a $ParA_F$ dimer could belong to one $ParB_F$
339 dimer as seen in the absence of CTP or *parS*$_F$ (Figure 4A-B and 7B middle). However, most $ParB_F$
340 dimers in partition complexes *in vivo* would be CTP-bound and *parS*$_F$-activated, spreading over a
341 *parS*$_F$-proximal DNA region. CTP or *parS*$_F$ binding alters the $ParB_F$ dimer structure to prevent a
342 single $ParB_F$ dimer from providing both copies of the N-terminal domain to occupy both binding
343 faces of a $ParA_F$ dimer, necessitating two $ParB_F$ dimers, each providing one N-terminal domain to
344 a $ParA_F$ dimer (Figure 4C-D, 5 and Figure 7B bottom). Strikingly, *parS*$_F$ together with CTP
345 significantly increased the A_2B_4 complex assembly rate on nsDNA without affecting its
346 disassembly rate. Although we have not analyzed the kinetic details of the process that leads to the
347 ATPase activation by $ParB_F$, we propose a moderately slow transition separates formation of the
348 ATPase-activated A_2B_4 complex from rapidly reversible $ParA_F$—$ParB_F$ interaction processes. Such
349 a local slow step would partially decouple the reversible $ParA_F$—$ParB_F$ interaction dynamics from
350 the irreversible ATP hydrolysis, thereby promoting dynamic interactions between the nucleoid and
351 partition complex that facilitate partitioning *via* the diffusion-ratchet mechanism as elaborated
352 below.

353 Figure 7. *Cartoon of the proposed pre-ATPase-activation complexes of $ParA_F$ and $ParB_F$.*

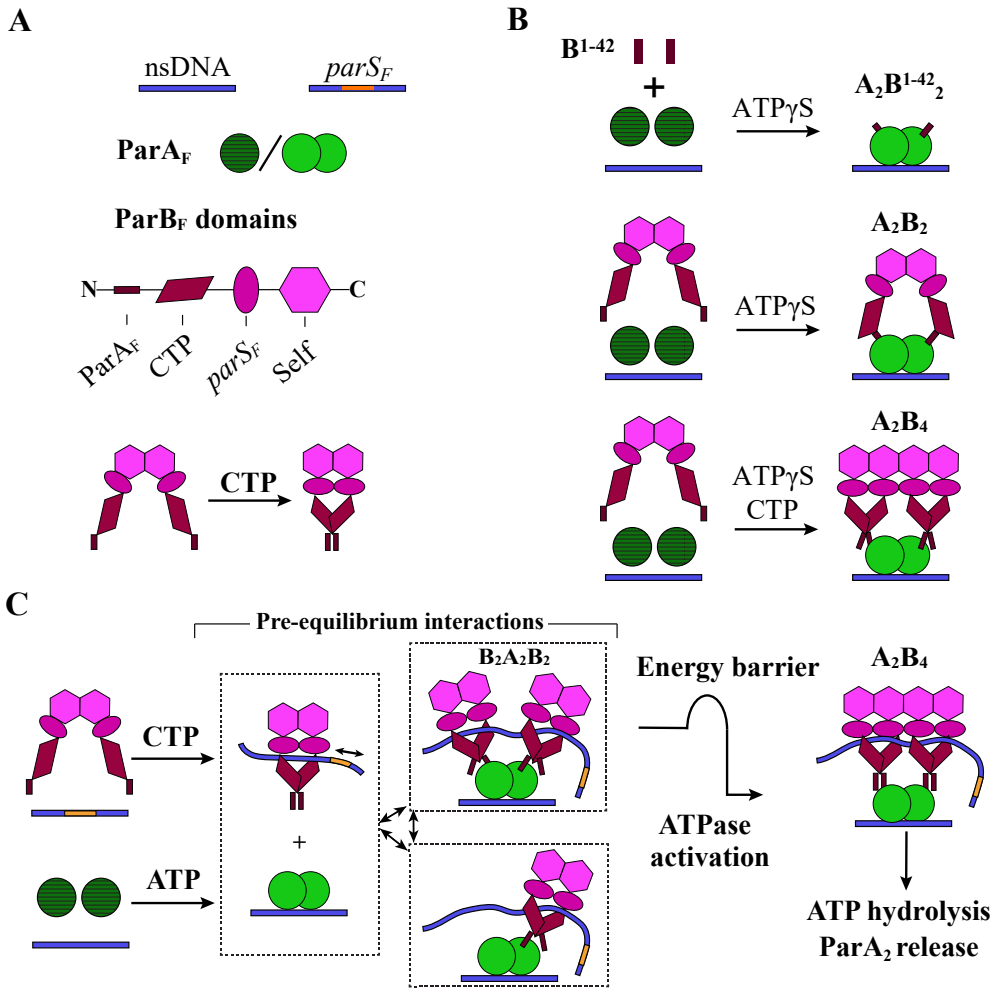

Figure 7. (A) Pictograms of nsDNA, *$parS_F$*-DNA, $ParA_F$ monomer/dimer and $ParB_F$ domains with binding ligand designations. The CTPase domains of a $ParB_F$ dimer fold forming a single globular domain by binding CTP bringing the two $ParA_F$-binding domains to close proximity. (B) $ParA_F$-binding domain, $ParB_F^{1\text{-}42}$ by itself can convert $ParA_F$ monomers to DNA-binding-competent dimers in the presence of ATPγS by forming an $A_2B^{1\text{-}42}{}_2$ complex (top). $ParB_F$ dimers in the absence of CTP (or CDP) convert $ParA_F$ monomers to DNA-binding-competent dimers in the presence of ATPγS by straddling a $ParA_F$ dimer to form an A_2B_2 complex (middle). In the presence of CTP, the close proximity of the $ParA_F$-binding domains of the $ParB_F$ dimer prevents A_2B_2 complex formation and instead A_2B_4 complex assembles on nsDNA in the presence of

ATPγS (bottom). (C) In the presence of *parS*$_F$ and CTP, ParB$_F$ dimers load on to the *parS*$_F$-DNA and spread to adjacent DNA regions while adopting a state that enables faster assembly of A_2B_4 complexes. Considering the requirements for efficient partition complex motion by diffusion-ratchet mechanism based on the chemophoretic principle of force generation, we propose a significant energy barrier that slows the formation of the ATP hydrolysis-competent A_2B_4 complex. This energy barrier partially decouples ParA$_F$—ParB$_F$ association-dissociation dynamics from ATP hydrolysis, which triggers ParA$_F$ dissociation from the nucleoid.

354 The clearest indication that both $ParB_F$-interacting faces of the nsDNA-bound $ParA_F$ dimer must
355 be occupied by the N-terminal domain of $ParB_F$ for ATPase activation came from experiments
356 using artificial $ParB_F$ constructs. We showed that monomeric $ParB_F^{1-42}$ stimulates $ParA_F$ ATPase
357 with a clear sigmoidal concentration dependence, indicating that one molecule of $ParB_F^{1-42}$ binding
358 to one side of a $ParA_F$ dimer cannot fully activate the $ParA_F$ ATPase (Figure 2F). When ATP
359 hydrolysis was blocked by using non-hydrolysable ATPγS, $ParB_F^{1-42}$-mCherry formed an
360 equimolar complex with $ParA_F$ dimers (Figure 2C). Thus, the $ParA_F$ forms a complex with $ParB_F^{1-}$
361 ^{42}-mCherry bound at both $ParB_F$-interacting faces of the $ParA_F$ dimer prior to ATP hydrolysis (Fig
362 7B; top). Consistently, an artificially dimeric $ParB_F^{1-42}$ construct, $ParB_F^{1-42}$-mCherry-$EcoRI^{E111Q}$,
363 efficiently activated $ParA_F$-ATPase with hyperbolic concentration dependence (Figure 2G).

364 In the absence of CTP or *parS*$_F$, the $ParB_F$ dimer is held together by the C-terminal self-
365 dimerization domain (Fig 7A bottom) with dimerization K_d of ~19 nM (Figure 4—figure
366 supplement 1). In this state, the N-terminal half of the protein is thought to be mostly unfolded.
367 Thus, one dimer could straddle a $ParA_F$-dimer with the two N-terminal $ParA_F$-interaction domains
368 interacting the two faces of a $ParA_F$-dimer (Figure 7B middle).

369 In contrast, when bound by CTP or CDP the CTPase domains in a $ParB_F$ dimer fold to form a
370 single globular domain (Figure 7A bottom) (Soh et al., 2019). The two $ParA_F$-interaction domains
371 emanating from this folded domain are unlikely to reach both sides of a $ParA_F$ dimer, necessitating
372 an A_2B_4 complex for ATPase activation (Figure 7B bottom). In theory, it is possible that a chain
373 of $(A_2B_2)_n$ might form, but the 1:2 protein stoichiometry observed in the presence of ATPγS
374 indicates such a configuration is unfavored. A_2B_4 complexes formed in the presence of CTP and

375 *parS$_F$* DNA fragments contained almost no *parS$_F$* DNA fragments (Figure 5E). This is consistent
376 with the notion that after binding *parS$_F$*, CTP-ParB$_F$ dimers convert to a low *parS$_F$*-affinity state
377 while remaining topologically bound to the DNA and spreading to surrounding DNA regions (Soh
378 et al., 2019).

379 Even in the absence of C-nucleotides, addition of *parS$_F$* promotes the formation of an A_2B_4
380 complex (Figure 4C, D). It is possible that when a ParB$_F$ dimer binds *parS$_F$*, the adjacent residues
381 that constitute the CTPase domains of the two monomers adopt a mutually interacting folded state
382 akin to the C-nucleotide-bound state even in the absence of the nucleotide as noted by Soh, et al.
383 (2019). This may prevent formation of the A_2B_2 complex, favoring the A_2B_4 complex that was
384 observed. Consistent with this interpretation, the shift from A_2B_2 to A_2B_4 complex by the addition
385 of *parS$_F$* did not occur with the Box II mutant ParB$_F^{R121A}$, which is expected to be unable to form a
386 stable nucleotide-binding fold (Figure S8). Even in the absence of CTP, the A_2B_4 complex formed
387 in the presence of *parS$_F$* DNA fragment contained significantly less than a stoichiometric amount
388 of *parS$_F$* fragment (Figure 5E). This suggests that association with nsDNA-bound ParA$_F$ dimer
389 lowers the affinity of ParB$_F$ for *parS$_F$*.

390 All the A_2B_2 and A_2B_4 complexes we observed in the presence of ATPγS dissociated from nsDNA
391 more slowly (k_{off} = 0.5 - 1 min^{-1}; Supplementary Table 1) compared to ParA$_F$ in the absence of
392 ParB$_F$ (~6 min^{-1}; Fig 2B). For the case of monomeric ParB$_F^{1-42}$, which dissociated from ParA$_F$ more
393 rapidly, the presence of 10 μM ParB$_F^{1-42}$ in the wash buffer restored the low apparent nsDNA
394 dissociation rate constant of the complex (Figure 2E). Nevertheless, ParA$_F$ dimers in these
395 complexes appear to be primed for further conformational change toward less stably DNA-

396 associated state. Upon dissociation of $ParB_F^{1-42}$ from the $A_2B^{1-42}{}_2$ complex, $ParA_F$ dissociated from
397 the DNA-carpet within a second or so, much faster than the ATPγS-$ParA_F$-dimer that has not yet
398 formed a A_2B_2 or A_2B_4 complex (Figure 2D, 3B).

399 Our single-molecule DNA condensation measurements indicate that CTP-bound $ParB_F$ dimers are
400 activated by contacting $parS_F$ to load *in cis* onto the $parS_F$-carrying DNA in numbers exceeding
401 the copy number of the $parS_F$-consensus sequence (ParB spreading) as shown by others for
402 chromosomal ParBs (Jalal et al., 2020; Soh et al., 2019), and condense the DNA forming an *in*
403 *vivo* partition complex-like structure (Figure 6). CDP-bound $ParB_F$ dimers were inefficient in
404 condensing $parS_F$-carrying DNA and the condensation observed was disrupted far more readily
405 than CTP-supported condensates, indicating $ParB_F$-CDP dimers do not efficiently load onto the
406 DNA tether in a state capable of DNA-condensation (Figure 6, Figure 6—figure supplement 1B).
407 Our results show that DNA-condensation is caused by $ParB_F$-$ParB_F$ interactions forming DNA-
408 looping bridges without requiring other protein factors. Combined with evidence for a unique
409 conformational state of the $parS_F$-activated $ParB_F$-CTP, we favor the view that DNA-bridging
410 capability, mediated by $ParB_F$-$ParB_F$ binding, is another attribute of this state of $ParB_F$.

411 Evidence indicates that $parS_F$ interactions induce a unique conformational state in CTP-bound
412 $ParB_F$ dimers that promotes spreading, which retains this conformational state even after freed
413 from $parS_F$-containing DNA. $ParB_F$ associates with nsDNA-bound $ParA_F$ dimers forming the A_2B_4
414 complex with a faster apparent assembly rate in the presence of $parS_F$ and CTP together than with
415 either CTP or $parS_F$ alone. This observation is consistent with the decreased half-saturation
416 concentration in the ATPase activation assay (Figure 5G, Table 2). According to the sliding clamp

417 model of the spreading ParB-CTP dimers proposed by Soh et al., (2019), $ParB_F$-CTP dimers loaded
418 onto a short *$parS_F$* DNA fragments would quickly slide off the DNA as shown by Jalal et al., (2020).
419 Since our ATPase activation assay and the DNA-carpet-bound A_2B_4 complex assay in the presence
420 of CTP and *$parS_F$* were done using a short linear *$parS_F$* DNA fragment, the *$parS_F$*-activated state
421 of the $ParB_F$-CTP dimers we described in this study must remain in this "activated" state for an
422 extended period after sliding off the *$parS_F$* fragment. Accordingly, the A_2B_4 complexes bound to
423 the DNA-carpet in the presence of CTP, ATPγS and *$parS_F$* fragments contained almost no *$parS_F$*
424 fragments (Figure 5E). Thus, *$parS_F$* acts as a catalyst to convert $ParB_F$-CTP dimers from a pre-
425 activation state to an activated state capable of faster A_2B_4 complex assembly. Although the $ParB_F$
426 dimers in this activated state failed to load efficiently onto DNA lacking *$parS_F$* sequences *in trans*
427 (Figure 6—figure supplement 2), in the absence of contrary evidence, the parsimonious
428 assumption is that this $ParB_F$ dimer retains the conformation of spreading $ParB_F$ dimers that remain
429 loaded on the *$parS_F$*-containing DNA *in cis*, the majority of $ParB_F$ dimers in the partition complexes
430 *in vivo*. Thus, we propose that the functional properties of $ParB_F$ we observed in the presence of
431 CTP and *$parS_F$*, both in facilitating assembly of A_2B_4 complexes and activating $ParA_F$-ATPase,
432 reflect those of the majority of $ParB_F$ dimers in partition complexes *in vivo*.

433 Our study, together with previous studies, indicates that the ATP turnover rates of ParABS systems
434 are slow because of multiple, slow kinetic steps. These slow steps are strategically placed in the
435 reaction pathway in order to tune the system and drive the motion of the partition complex by the
436 diffusion-ratchet mechanism (Sugawara and Kaneko, 2011; Vecchiarelli et al., 2010). Even at
437 saturating concentrations of $ParB_F$ in the *$parS_F$*-activated CTP-bound state, the maximum ATP
438 turnover rate of $ParA_F$ remained modest (~80 ATP/$ParA_F$-monomer/hour; Fig 5). The slow

439 reactivation of ParA nucleoid binding after ATP hydrolysis dominates the overall ATPase cycle
440 time (Vecchiarelli et al., 2010). The presence of a large fraction of $ParA_F$ in an unbound state
441 during the steady state ATPase assay was evidenced by the fact that the half-saturation
442 concentration of $ParB_F$ (in the presence of CTP and *parS*$_F$) forming the A_2B_4 complex was ~0.2
443 μM while the total $ParA_F$ concentration was 1 μM, suggesting less than ~20% of $ParA_F$ was in the
444 nsDNA-bound state ready to interact with $ParB_F$. *In vivo* the reactivation rate is likely lower since
445 nucleoid-bound ParA is only fully activated on encountering the partition complex, which lowers
446 the concentration of ParA in the cytosol waiting to be activated. The lower precursor concentration
447 slows the nucleoid rebinding rate of ParA non-linearly, because reactivation involves relatively
448 fast nucleotide-dependent ParA dimerization pre-equilibrium with apparent Kd of ~2 μM,
449 followed by a slow conformational step. This makes the process dimerization-limited at lower
450 precursor ParA concentrations according to the study of $ParA_{P1}$ (Vecchiarelli, 2010). Whereas this
451 slow ParA reactivation and rebinding process, which allows the maintenance of the nucleoid-
452 bound ParA concentration gradient (Hu et al., 2017), is a critical element of chemophoresis driven
453 motility, the rate of ParA-ATPase activation by ParB is another important factor. In particular,
454 efficient chemophoresis force generation relies on $ParA_F$—$ParB_F$ interactions achieving a local
455 quasi-equilibrium prior to ATP hydrolysis (Sugawara and Kaneko, 2011). Therefore, we speculate
456 that there is a significant energy barrier associated with the conformational transition of a $ParA_F$—
457 $ParB_F$ complex to achieve ATPase activation (Figure 7F). The resulting local time delay, in
458 addition to the fact that two ParB dimers are required to bind a ParA dimer to activate its ATPase,
459 would partially decouple the pre-ATP hydrolysis $ParA_F$—$ParB_F$ reversible interaction steps from
460 the ATP hydrolysis step. This delay would in turn permit ParB—ParA binding to approach local

461 quasi-equilibrium, increasing the efficiency of ParA distribution gradient sensing and motive force
462 generation by the partition complex. In addition, this slow activation step would prevent possible
463 over-depletion of the local nucleoid-bound $ParA_F$ as the partition complex establishes the $ParA_F$
464 depletion zone.

465 The disassembly of the ATP-bound A_2B_4 complex might be slow prior to ATP hydrolysis
466 considering the stability of the complexes in the presence of ATPγS. Thus, we propose the energy
467 barrier postulated above is positioned immediately prior to formation of this complex rather than
468 between this complex assembly and ATP hydrolysis. A slow step after formation of the stable
469 complex would prolong the lifetime of the link between the nucleoid and the partition complex
470 impeding the partition complex motion without permitting the reversible $ParA_F$—$ParB_F$ interaction
471 to approach equilibrium. We consider this conformational transition likely is the step
472 synergistically accelerated by CTP and $parS_F$. We note that the CTP-bound and $parS_F$-activated
473 $ParB_F$ activates $ParA_F$ ATPase with clear sigmoidal concentration dependence (Figure 5G, Table
474 2) suggesting two $ParB_F$ dimers separately bind a $ParA_F$ dimer during pre-equilibrium binding
475 phase forming transient $B_2A_2B_2$ complex. We imagine the slow conformational step proposed here
476 might be assisted by the property of the CTP/$parS_F$-activated $ParB_F$ dimers that promotes inter-
477 dimer interactions as suggested by the magnetic tweezers experiments, stabilizing the interaction
478 between the two $ParB_F$ dimers within a complex, depicted as conversion of $B_2A_2B_2$ complex to
479 A_2B_4 complex in Figure 7C. This might explain its higher assembly rate by the $parS_F$-activated
480 $ParB_F$-CTP and slightly increased stability of the complex. Yet, CTP and $parS_F$ DNA do not
481 significantly increase the ATP turnover number of ~80 h^{-1}, indicating that the proposed kinetic
482 delay time cannot be more than a few seconds. Assembly of $A_2B^{1\text{-}42}{}_2$ complex perhaps does not

483 experience this time delay due to less steric constraints, but $ParB_F^{1-42}$ dissociates more readily. Not
484 all the conditions we tested for ATPase activation by the formation of A_2B_4 complexes exhibited
485 clearly sigmoidal $ParB_F$ concentration dependence (Figures 4, Table 2). This could reflect
486 differences in the kinetic step and/or magnitude of the cooperative interactions between the two
487 $ParB_F$ (dimers) binding nsDNA-bound $ParA_F$ dimers along the assembly path of the $A_2B_{2/4}$
488 complex under different cofactor and $ParB_F$ mutation conditions.

489 This study demonstrates how *parS*$_F$, along with CTP, has wide-reaching roles in the F-plasmid
490 ParABS system; not only in $ParB_F$'s ability to spread from *parS*$_F$ and promote $ParB_F$—$ParB_F$
491 interactions for partition complex compaction, but also in $ParB_F$ dimer interactions with $ParA_F$.
492 However, in order to understand how the system is fine-tuned to achieve system dynamics that
493 result in robust plasmid segregation, improved understanding of the microscopic kinetic
494 parameters is essential. Many details of the system dynamics remain to be addressed to understand
495 the full picture of the ParABS partition mechanism.

496 **Materials and Methods**

497 *Plasmids and constructs for protein expression.*

498 All expression open reading frames were synthesized and subcloned into pET11a (Genscript).
499 $ParA_F$, $ParA_F$-eGFP, $ParB_F$, $ParB_F^{R121}$, $ParB_F^{1-42}$-mCherry, $ParB_F^{1-42\ R36A}$-mCherry and $ParB_F^{1-42}$-
500 mCherry-$EcoRI^{E111Q}$ constructs were made with a hexa-histidine tag on their C-terminus. Protein
501 fusions were made with a SGGG linker between fused domains, with exception of $ParB_F^{1-42}$-
502 mCherry-$EcoRI^{E111Q}$ which had a 4x (SGGG) linker between $ParB_F^{1-42}$ and mCherry. $ParB_F^{1-42}$ and
503 $ParB_F^{1-42\ R36A}$ were synthesized *de novo* (Genscript).

504 *Oligonucleotides.*

505 The 24 bp double-stranded DNA fragments containing the $parS_F$ consensus sequence and a
506 scrambled sequence used in this study were: 5'-AGT CTG GGA CCA CGG TCC CAC TCG; 5' -
507 AGT CTG CAG CTA CTA TAC CAC TCG, respectively and their complements. The
508 fluorescently labelled $parS_F$ substrate was synthesized with Alexa-488 NHS coupled to the 5' of
509 the forward strand by the manufacturer (IDT).

510 *Protein purification and fluorescent labelling.*

511 For expression of proteins 5 ml of an overnight culture of BL21 DE3 AI (Invitrogen) *E. coli* cells
512 transformed with the desired plasmid were inoculated into 500 ml Terrific Broth (Teknova)
513 supplemented with 100 µg/ml carbenicillin, antifoam Y-40 emulsion (Sigma), 1 g/l NaCl, 0.7 g/l
514 Na_2SO_4, 2.6 g/l NH_4Cl, and 0.24 g/l $MgSO_4$. The cultures were incubated at 37 °C in 2.5 l Fernbach

515 flasks and shaken at 120 rpm until they reached an OD_{600} of 1.8. Cultures were chilled on ice before
516 they were induced by the addition of 1 mM IPTG and 0.2 % L-arabinose. Following induction,
517 cultures were incubated at 16 °C for 16 hr and cells were harvested by centrifugation at 6000 x g
518 for 15 min at 4 °C. Cell pellets were frozen in liquid nitrogen and stored at -80 °C.

519 Frozen cells were thawed and resuspended to a density of 1 g cell pellet/10 ml in lysis buffer
520 ($ParA_F$, $ParA_F$-eGFP and $ParB_F^{1-42}$-mCherry-$EcoRI^{E111Q}$: 25 mM Tris.HCl pH 8, 1 M NaCl, 20 mM
521 imidazole, 2 mM β-mercaptoethanol, 10% glycerol; $ParB_F$ and $ParB_F^{R121A}$: 10 mM Sodium
522 Phosphate buffer pH 7, 1 M NaCl, 20 mM Imidazole , 2 mM β-mercaptoethanol, 10% glycerol;
523 $ParB_F^{1-42}$-mCherry and $ParB_F^{1-42/R36A}$-mCherry: 25 mM HEPES.KOH pH 7.5, 150 mM NaCl, 6 M
524 guanidinium chloride, 20 mM Imidazole, 2 mM β-mercaptoethanol, 10% glycerol) containing
525 EDTA-free Sigmafast protease inhibitor cocktail tablet (Sigma) using a homogenizer. Lysozyme
526 and Benzonase (Sigma) were added to a concentration of 1 mg/ml and 50 u/ml, respectively, and
527 the cells were lysed *via* a microfluidizer. Cell debris were pelleted by centrifugation at 142,000 x
528 g for 45 min at 4 °C, and the supernatant passed through a 0.22 μm filter.

529 Lysate was loaded on to a 5 ml HisTrap HP cassette (GE Healthcare) equilibrated in lysis buffer.
530 The cassette was then washed with 10 column volumes of lysis buffer followed by 10 column
531 volumes HisTrap buffer (as lysis buffer without guanidinium hydrochloride and with the following
532 NaCl concentrations: $ParA_F$ proteins, 200 mM; $ParB_F$ proteins, 150 mM), and the protein eluted
533 with a gradient from 20 to 500 mM imidazole over 10 column volumes using an AKTA Pure (GE
534 Healthcare).

535 All proteins except $ParB_F^{1-42}$-mCherry and $ParB_F^{1-42\ R36A}$-mCherry were then subjected to ion-
536 exchange chromatography. The peak fractions from the HisTrap column were pooled and slowly
537 diluted whilst stirring with a Mono Q/S-buffer (as lysis buffer without imidazole or NaCl, but with
538 0.1 mM EDTA pH 8) until the conductivity of the sample was: 18 mS/cm for $ParA_F$ proteins, 5
539 mS/cm for $ParB_F^{1-42}$-mCherry-$EcoRI^{E111Q}$ and 15 mS/cm for all other $ParB_F$ proteins. The
540 conductivity of the samples was monitored using a conductivity meter (Hanna). The sample was
541 loaded onto either a 1-ml Mono Q ($ParA_F$ proteins and $ParB_F^{1-42}$-mCherry-$EcoRI^{E111Q}$) or Mono S
542 (other $ParB_F$ proteins) 5/50 GL ion exchange column (GE Healthcare) pre-equilibrated with Mono
543 Q/S-buffer containing a NaCl concentration to match the conductivity of the sample. The column
544 was then washed with 10 column volumes of Mono Q/S-buffer + NaCl. The protein was eluted
545 with a gradient up to 500 mM NaCl over 10 column volumes.

546 Finally, all protein samples were purified by size-exclusion chromatography. The peak fractions
547 from the previous column were pooled and diluted 50:50 with concentration buffer (25 mM
548 HEPES.KOH pH 7.5, 2 M NaCl, 2 mM β-mercaptoethanol, 10% glycerol) and concentrated to ~2
549 ml using a Centriprep 10-KDa spin concentrator (Millipore). The sample was then injected onto
550 an S200 16/600 size exclusion column (GE Healthcare) pre-equilibrated in gel filtration buffer (25
551 mM HEPES-KOH pH 7.5, 0.1 mM EDTA pH 8, 0.5 mM TCEP and 10% glycerol with 600 mM
552 KCl for $ParA_F$ proteins and 150 mM KCl for $ParB_F$ proteins). Peak fractions were then pooled and
553 concentrated to ~100 μM (~5-10 mg/ml) as determined by UV 280 nm absorbance before being
554 aliquoted, frozen in liquid nitrogen and stored at –80 °C. Protein aliquots were used once and not
555 subjected to freeze-thaw cycles.

556 To produce fluorescently labeled $ParB_F$ and $ParB_F^{R121A}$, $ParB_F$ protein was buffer exchanged into
557 gel filtration buffer without reducing agent and incubated with a two-molar excess of Alexa Fluor
558 647 C2 Maleimide (Thermo Fisher) for 30 min at room temperature. The reaction was then
559 quenched by the addition of DTT to a final concentration of 10 mM. The protein solution was then
560 filtered through a 0.22 μm filter and free dye removed by buffer exchange into gel filtration buffer
561 in Amicon ultra 10 KDa spin concentrator (Millipore). The extent of labeling was monitored based
562 on absorbance at 280 and 647 nm.

563 *Assaying contaminating activities in the protein preparations.*

564 Proteins purified by the above protocol had no significant DNA endonuclease activity. After 16 hr
565 incubation of supercoiled pBR322 with 2 μM $ParA_F$ and/or 10 μM $ParB_F$ at 37 °C in ATPase buffer
566 (see below) no linear DNA was observed and less than 10% of the supercoiled plasmid was
567 converted to a nicked-circular form. The contaminating ATPase activity for all $ParB_F$ proteins was
568 less than two mol ATP per mol $ParB_F$ per hour, as determined by the ATPase assay protocol
569 detailed below.

570 *ATPase activity assays.*

571 Steady-state ATPase activity was measured as described (Vecchiarelli et al., 2016) with
572 modifications. ATP to be used for ATPase activity assays was purified after diluting 20 μCi ATP
573 γ-P^{32} (Perkin-Elmer) in 100 μl of 100 mM unlabeled ATP (Sigma) by passing through a 3 ml P2
574 resin size-exclusion column equilibrated with a buffer containing 50 mM HEPES·KOH pH 7.5,
575 150 mM KCl and 0.1 mM EDTA. The purity of fractions was determined by TLC. 1 μl of each

576 fraction was spotted on to a 10 x 8 cm piece of TLC PEI Cellulose F paper (Millipore) 1 cm above
577 the bottom of the paper and developed for 10 mins using 400 mM NaH_2PO_4 pH 3.6 as the solvent.
578 The fractions containing the minimum contamination of P^{32}-Pi were pooled and their concentration
579 determined by spectrometry before storage at -20 °C.

580 $ParA_F$ ATPase activity was measured in the presence of the combinations and concentrations of
581 proteins and DNA cofactors specified in the main text in ATPase buffer (50 mM HEPES·KOH pH
582 7.5, 150 mM KCl, 5 mM $MgCl_2$, 0.5 mM TCEP and 1 mM ATP γ-P^{32}). Reactions were incubated
583 at 37 ºC for 4 hrs and stopped by the addition of an equal volume of 1 M formic acid. The increase
584 of P^{32}-Pi was measured by TLC using PEI Cellulose F paper as detailed above.

585 *TIRF microscopy*.

586 The general design of the TIRF microscopy setup was essentially as previously described (Ivanov
587 and Mizuuchi, 2010; Vecchiarelli et al., 2013). A prism-type TIRFM system was built around an
588 Eclipse Ti microscope (Nikon) with a 40x objective (S Fluor, 40x/1.30 oil, Nikon) and two-color
589 images captured by an Andor DU-897E camera through a dxcr630 insert DualView (Photometrics)
590 with the following settings: 3 MHz digitizer (grey-scale); 5.2 pre-amplifier gain, 2 MHz vertical
591 shift speed; +1 vertical clock range; electron-multiplying gain 30; EM CCD temperature set at -90
592 ºC; baseline clamp ON; and exposure time 100 ms.

593 The excitation for $ParA_F$-eGFP and Alexa647-$ParB_F$ were provided by a 488 nm diode-pumped
594 solid-state laser (Sapphire, Coherent) and a 633 nM HeNe laser (Research Electro-Optics),
595 respectively. The TIRF illumination had an elliptical Gaussian shape in the field of view therefore

596 intensity data for DNA-carpet-bound $ParA_F$-eGFP and Alexa647-$ParB_F$ signals were taken at or
597 near the middle of the illumination profile.

598 Movies were acquired using Metamorph 7 (Molecular Devices) and transferred to ImageJ
599 (National Institutes of Health) for analysis.

600 Flow cells were assembled using fused silica microscope slides with pre-drilled inlet/outlet ports
601 (Esco products), #1 glass cover slips (24 x 50 mm, Thermo Fisher) and 0.001”-thick acrylic
602 transfer tape (3M). The fused silica slide was cleaned by soaking overnight in a solution of
603 Nochromix (Sigma)-sulfuric acid, followed by extensive rinsing with de-ionized water, drying by
604 blowing nitrogen gas, followed by oxygen plasma treatment (South Bay Technology Inc). The Y-
605 shaped flow path pattern was cut out of the transfer tape using a laser cutter before the flow cell
606 assembly. Nanoports (Idex) were attached to the fused silica slide for the inlet and outlet tube
607 connections using Norland Optical Adhesive (Thorlabs), cured by 365 nm UV light. The
608 assembled flow cells were then baked at 80 °C with gentle compression for 2 hr.

609 To assemble a DNA-carpet in a flow cell, small unilamellar vesicles (SUVs) of 1,2-dioleoyl-*sn*-
610 glycero-3-phosphocholine (DOPC) and 1,2-dioleoyl-*sn*-glycero-3-phosphoethanolamine-N-
611 (biotinyl) (DOPE-Biotin) (Avanti Polar Lipids) were prepared as follows. 0.5 ml of DOPC (25
612 mg/ml chloroform) was mixed with 5 µl of DOPE-biotin (25 mg/ml chloroform) in a glass test
613 tube and most of the solvent removed *via* evaporation under a nitrogen flow. The remaining solvent
614 was removed by drying in a SpeedVac (Savant) at 42 °C for 1 hr followed by a further 1 hr at room
615 temperature. 2.5 ml of degassed TK150 buffer (25 mM Tris.HCl pH 7.5, 150 mM KCl) was then
616 added and the lipids stored, covered under nitrogen gas overnight. The lipids were then

617 resuspended by vortexing and sonicated (70-80 watts, 30 sec on, 10 sec off) in a cup horn with
618 water chiller set to 16 °C (QSonica) until transparent. The resulting solution of SUVs was then
619 filtered through a 0.22 μm filter, aliquoted and stored under nitrogen gas at 4 °C for up to 4 weeks.

620 To prepare biotinylated salmon sperm DNA for DNA-carpets 10 mg/ml salmon sperm DNA
621 (Thermo Fisher) was sonicated for 5 min (110 watts, 10 sec on, 10 sec off) to produce short
622 fragments. Sonicated salmon sperm DNA was then diluted to 1 mg/ml in Terminal Transferase
623 buffer (NEB) with 0.25 mM $CoCl_2$, 40 μM Biotin-14-dCTP (Thermo Fisher) and 1 unit/μl
624 Terminal Transferase (NEB). The DNA was incubated at 37 °C for 30 min, then the reaction
625 stopped by heat inactivation at 75 °C for 20 min. Free Biotin-14-dCTP was removed by extensive
626 buffer exchange with TE buffer (10 mM Tris.HCl pH 8, 0.1 mM EDTA) in a 100 kDa Amicon
627 Ultra spin concentrator (Millipore). The biotinylated DNA was then concentrated to ~10 mg/ml
628 and stored at -20 °C until needed.

629 To assemble a DNA-carpet, the DOPC—DOPE-biotin SUV solution was diluted to 1 mg/ml in
630 500 μl degassed TN150MC buffer (25 mM Tris.HCl pH7.5, 150 mM NaCl, 5 mM $MgCl_2$, 0.1 mM
631 $CaCl_2$) and warmed to 37 °C. Approximately 300 μl of SUV solution was then infused into a pre-
632 warmed flow cell and incubated at 37 °C for 1 hr. Excess SUVs were washed out with 500 μl
633 warmed, degassed TN150MC buffer at 100 μl/min. 300 μl of a solution of 1 mg/ml neutravidin
634 (Thermo Fisher) in warmed, degassed TN150MC buffer was then infused at a rate of 100 μl/min
635 into the flow cell and incubated at 37 °C for 30 min. Excess neutravidin was washed out with
636 TN150MC buffer as above, and the flow cell infused with 100 μl of a solution containing 1 mg/ml
637 biotinylated sonicated salmon sperm DNA (as prepared above) in warmed, degassed TN150MC

638 buffer and incubated at 37 °C for 30 min. The ports of the flow cell were sealed with parafilm and
639 stored at 4 °C for up to a week.

640 Prior to use, excess DNA was removed by infusion of 300 µl 0.22 µm filtered and degassed TIRFM
641 buffer (50 mM HEPES.KOH pH 7.5, 300 mM K-glutamate, 50 mM NaCl, 10 mM $MgCl_2$, 0.1 mM
642 $CaCl_2$, 2 mM DTT, 0.1 mg/ml α-casein, 0.6 mg/ml ascorbic acid, 10% glycerol) with addition of
643 1 mg/ml α-casein and 1 mM ATPγS and the flow cell incubated at room temperature for 30 min.

644 Conversion of the fluorescence signal detected in TIRF microscopy to the DNA-carpet-bound
645 protein densities was done following the procedure described in the legend of Figure S4 in
646 (Vecchiarelli et al., 2016).

647 *Fluorescence Recovery After Photobleaching (FRAP).*

648 For FRAP experiments, 488 nm solid-state and 630 nm diode laser was focused to the back focal
649 plane of the objective through an appropriate dichroic mirror (Di01-R405/488/561/635-25x36,
650 Semrock) through the objective lens to illuminate a ~5 or ~10 µm (for 488 nm or 630 nm,
651 respectively) diameter spot in the center of the sample area. The laser power was adjusted for
652 ~80 % bleaching with 5 s exposure for the eGFP or Alexa 647 signals, and four cycles of
653 bleaching/recovery were recorded for each sample and averaged.

654 *Magnetic Tweezers-based DNA condensation assay.*

655 The magnetic tweezer setup and assays conducted with it were performed as previously described
656 (Seol and Neuman, 2011; Seol et al., 2016).

657 The ability of $ParB_F$ to condense *parS*$_F$-containing DNA (spDNA) was tested by a custom-built
658 magnetic tweezer setup. In brief, two permanent magnets were used to apply force to micron sized
659 magnetic beads individually tethered to the coverslip of a one inlet flow cell by 5 kb pET28a
660 plasmid-derived DNA tethers. The distance the magnets were held from the beads, and hence the
661 force exerted upon them, was controlled by a linear motor that vertically positions the magnets.

662 5kb DNA substrates were generated by PCR using either pET28a-*parS*$_F$ plasmid (for *parS*$_F$-
663 containing DNA) or pET28a as templates. pET28-*parS*$_F$ DNA plasmid was generated by cloning
664 570 bp DNA segment containing 12 repeats of *parS*$_F$ native sequence from F-plasmid into pET28a
665 between the BamHI and SphI restriction sites.

666 Primers used for the PCR contained an extra non-complementary 15 nt at their 5' ends to encode
667 BsaI restriction sites. The PCR reaction yields a 5.2 kb product incorporating two BsaI restriction
668 sites at its termini. Digestion of this product was followed by ligation with 500 bp DNA "handles"
669 containing either multiple biotin or digitoxin labels. These handles were also generated by Taq-
670 based PCR using pBlueScript II KS as the template, pBlueScript II KS forward (5'- GCT GGG
671 TCT CGG TTG TTC CCT TTA GTG AGG GTT AAT TG) and pBlueScript II KS reverse (5'-
672 GCT GGG TCT CGT GGT TTC CCT TTA GTG AGG GTT AAT TG) primers and either 60 μM
673 biotin-16-dUTP or digoxigenin-11-dUTP (Roche). This results in a 5 kb DNA tether which can be
674 attached to a streptavidin coated magnetic bead at one end and an anti-digoxigenin coverslip
675 surface at the other.

676 $ParB_F$ samples were prepared in modified ATPase buffer (50 mM HEPES.KOH pH 7.5, 100 mM
677 KCl, 5 mM $MgCl_2$, 2 mM DTT, 10 mg/ml BSA and 0.1% Tween-20) and infused into a flow cell

containing tethered magnetic beads held at 5 pN of force. After the chamber was filled, the flow was stopped, and the force reduced to 0.05 pN. The height of beads was tracked by analysis of diffraction rings generated by illumination of the beads from above and observed with an objective positioned below the flow cell. The extent of condensation by ParB was monitored by the decrease in the height of the beads at 0.05 and 5 pN as compared to controls without protein.

Acknowledgements

We are grateful to helpful suggestions and discussion of our colleagues Barbara Funnell, Michiyo Mizuuchi, Andrea Volante, Min Li, Masaki Osawa, William Carlquist and Shannon Mckie, and to Esme Neuman for help in preparation of figure 7. We thank Stephan Gruber and his colleagues for sharing their findings with us prior to publication. This work was supported by the intramural research fund for National Institute of Diabetes and Digestive and Kidney Diseases (K.M.); the National Heart, Lung, and Blood Institute (K.C.N.), National Institutes of Health, Department of Human Services.

JAT, KCN and KM conceived project, JAT and YS carried out experiments, JAT, YS, KCN and KM wrote manuscript.

694 **References**

695 Ah-Seng, Y., Lopez, F., Pasta, F., Lane, D., and Bouet, J.Y. (2009). Dual role of DNA in regulating
696 ATP hydrolysis by the SopA partition protein. J Biol Chem *284*, 30067-30075.

697 Ah-Seng, Y., Rech, J., Lane, D., and Bouet, J.Y. (2013). Defining the role of ATP hydrolysis in
698 mitotic segregation of bacterial plasmids. PLoS Genet *9*, e1003956.

699 Baxter, J.C., and Funnell, B.E. (2014). Plasmid Partition Mechanisms. Microbiol Spectr *2*.

700 Bouet, J.Y., Surtees, J.A., and Funnell, B.E. (2000). Stoichiometry of P1 plasmid partition
701 complexes. J Biol Chem *275*, 8213-8219.

702 Breier, A.M., and Grossman, A.D. (2007). Whole-genome analysis of the chromosome
703 partitioning and sporulation protein Spo0J (ParB) reveals spreading and origin-distal sites on the
704 Bacillus subtilis chromosome. Mol Microbiol *64*, 703-718.

705 Davey, M.J., and Funnell, B.E. (1994). The P1 plasmid partition protein ParA. A role for ATP in
706 site-specific DNA binding. J Biol Chem *269*, 29908-29913.

707 Davis, M.A., Martin, K.A., and Austin, S.J. (1992). Biochemical activities of the parA partition
708 protein of the P1 plasmid. Mol Microbiol *6*, 1141-1147.

709 Ebersbach, G., and Gerdes, K. (2004). Bacterial mitosis: partitioning protein ParA oscillates in
710 spiral-shaped structures and positions plasmids at mid-cell. Mol Microbiol *52*, 385-398.

711 Fung, E., Bouet, J.Y., and Funnell, B.E. (2001). Probing the ATP-binding site of P1 ParA: partition
712 and repression have different requirements for ATP binding and hydrolysis. EMBO J *20*, 4901-
713 4911.

714 Graham, T.G., Wang, X., Song, D., Etson, C.M., van Oijen, A.M., Rudner, D.Z., and Loparo, J.J.
715 (2014). ParB spreading requires DNA bridging. Genes & development *28,* 1228-1238.

716 Hatano, T., Yamaichi, Y., and Niki, H. (2007). Oscillating focus of SopA associated with
717 filamentous structure guides partitioning of F plasmid. Mol Microbiol *64*, 1198-1213.

718 Helsberg, M., and Eichenlaub, R. (1986). Twelve 43-base-pair repeats map in a cis-acting region
719 essential for partition of plasmid mini-F. J Bacteriol *165*, 1043-1045.

720 Hu, L., Vecchiarelli, A.G., Mizuuchi, K., Neuman, K.C., and Liu, J. (2017). Brownian Ratchet
721 Mechanism for Faithful Segregation of Low-Copy-Number Plasmids. Biophys J *112*, 1489-1502.

722 Ivanov, V., and Mizuuchi, K. (2010). Multiple modes of interconverting dynamic pattern
723 formation by bacterial cell division proteins. Proc Natl Acad Sci U S A *107*, 8071-8078.

724 Jalal, A.S., Tran, N.T., and Le, T.B. (2020). ParB spreading on DNA requires cytidine triphosphate
725 in vitro. eLife *9,* e 53515.

726 Le Gall, A., Cattoni, D.I., Guilhas, B., Mathieu-Demaziere, C., Oudjedi, L., Fiche, J.B., Rech, J.,
727 Abrahamsson, S., Murray, H., Bouet, J.Y., and Nollmann, M. (2016). Bacterial partition
728 complexes segregate within the volume of the nucleoid. Nat Commun *7*, 12107.

729 Leonard, T.A., Butler, P.J., and Lowe, J. (2005). Bacterial chromosome segregation: structure and
730 DNA binding of the Soj dimer--a conserved biological switch. EMBO J *24*, 270-282.

731 Lim, H.C., Surovtsev, I.V., Beltran, B.G., Huang, F., Bewersdorf, J., and Jacobs-Wagner, C.
732 (2014). Evidence for a DNA-relay mechanism in ParABS-mediated chromosome segregation.
733 eLife *3*, e02758.

734 Liu, W., Chen, Y., Watrob, H., Bartlett, S.G., Jen-Jacobson, L., and Barkley, M.D. (1998). N-
735 termini of EcoRI restriction endonuclease dimer are in close proximity on the protein surface.
736 Biochemistry *37*, 15457-15465.

737 Lutkenhaus, J. (2012). The ParA/MinD family puts things in their place. Trends Microbiol *20*,
738 411-418.

739 McLeod, B.N., Allison-Gamble, G.E., Barge, M.T., Tonthat, N.K., Schumacher, M.A., Hayes, F.,
740 and Barilla, D. (2017). A three-dimensional ParF meshwork assembles through the nucleoid to
741 mediate plasmid segregation. Nucleic acids research *45*, 3158-3171.

742 Mori, H., Mori, Y., Ichinose, C., Niki, H., Ogura, T., Kato, A., and Hiraga, S. (1989). Purification
743 and characterization of SopA and SopB proteins essential for F plasmid partitioning. J Biol Chem
744 *264*, 15535-15541.

745 Motallebi-Veshareh, M., Rouch, D.A., and Thomas, C.M. (1990). A family of ATPases involved
746 in active partitioning of diverse bacterial plasmids. Mol Microbiol *4*, 1455-1463.

747 Murray, H., Ferreira, H., and Errington, J. (2006). The bacterial chromosome segregation protein
748 Spo0J spreads along DNA from parS nucleation sites. Mol Microbiol *61*, 1352-1361.

749 Pillet, F., Sanchez, A., Lane, D., Anton Leberre, V., and Bouet, J.Y. (2011). Centromere binding
750 specificity in assembly of the F plasmid partition complex. Nucleic acids research *39*, 7477-7486.

751 Ravin, N.V., Kuprianov, V.V., Gilcrease, E.B., and Casjens, S.R. (2003). Bidirectional replication
752 from an internal ori site of the linear N15 plasmid prophage. Nucleic acids research *31*, 6552-6560.

753 Ringgaard, S., van Zon, J., Howard, M., and Gerdes, K. (2009). Movement and equipositioning of
754 plasmids by ParA filament disassembly. Proc Natl Acad Sci U S A *106*, 19369-19374.

755 Rodionov, O., Lobocka, M., and Yarmolinsky, M. (1999). Silencing of genes flanking the P1
756 plasmid centromere. Science *283*, 546-549.

757 Sanchez, A., Cattoni, D.I., Walter, J.C., Rech, J., Parmeggiani, A., Nollmann, M., and Bouet, J.Y.
758 (2015). Stochastic Self-Assembly of ParB Proteins Builds the Bacterial DNA Segregation
759 Apparatus. Cell Syst *1*, 163-173.

760 Scholefield, G., Whiting, R., Errington, J., and Murray, H. (2011). Spo0J regulates the oligomeric
761 state of Soj to trigger its switch from an activator to an inhibitor of DNA replication initiation. Mol
762 Microbiol *79*, 1089-1100.

763 Schumacher, M.A., and Funnell, B.E. (2005). Structures of ParB bound to DNA reveal mechanism
764 of partition complex formation. Nature *438*, 516-519.

765 Schumacher, M.A., Piro, K.M., and Xu, W. (2010). Insight into F plasmid DNA segregation
766 revealed by structures of SopB and SopB-DNA complexes. Nucleic acids research *38*, 4514-4526.

767 Seol, Y., and Neuman, K.C. (2011). Magnetic tweezers for single-molecule manipulation.
768 Methods Mol Biol *783*, 265-293.

769 Seol, Y., Strub, M.P., and Neuman, K.C. (2016). Single molecule measurements of DNA helicase
770 activity with magnetic tweezers and t-test based step-finding analysis. Methods *105*, 119-127.

771 Soh, Y.M., Davidson, I.F., Zamuner, S., Basquin, J., Bock, F.P., Taschner, M., Veening, J.W., De
772 Los Rios, P., Peters, J.M., and Gruber, S. (2019). Self-organization of parS centromeres by the
773 ParB CTP hydrolase. Science *366*, 1129-1133.

774 Song, D., Rodrigues, K., Graham, T.G.W., and Loparo, J.J. (2017). A network of cis and trans
775 interactions is required for ParB spreading. Nucleic Acids Res *45*, 7106-7117.

776 Sugawara, T., and Kaneko, K. (2011). Chemophoresis as a driving force for intracellular
777 organization: Theory and application to plasmid partitioning. Biophysics (Nagoya-shi) *7*, 77-88.

778 Taylor, J.A., Pastrana, C.L., Butterer, A., Pernstich, C., Gwynn, E.J., Sobott, F., Moreno-Herrero,
779 F., and Dillingham, M.S. (2015). Specific and non-specific interactions of ParB with DNA:
780 implications for chromosome segregation. Nucleic acids research *43*, 719-731.

781 Vecchiarelli, A.G., Han, Y.W., Tan, X., Mizuuchi, M., Ghirlando, R., Biertumpfel, C., Funnell,
782 B.E., and Mizuuchi, K. (2010). ATP control of dynamic P1 ParA-DNA interactions: a key role for
783 the nucleoid in plasmid partition. Mol Microbiol *78*, 78-91.

784 Vecchiarelli, A.G., Hwang, L.C., and Mizuuchi, K. (2013). Cell-free study of F plasmid partition
785 provides evidence for cargo transport by a diffusion-ratchet mechanism. Proc Natl Acad Sci U S
786 A *110*, E1390-1397.

787 Vecchiarelli, A.G., Li, M., Mizuuchi, M., Hwang, L.C., Seol, Y., Neuman, K.C., and Mizuuchi,
788 K. (2016). Membrane-bound MinDE complex acts as a toggle switch that drives Min oscillation
789 coupled to cytoplasmic depletion of MinD. Proc Natl Acad Sci U S A *113*, E1479-1488.

790 Vecchiarelli, A.G., Mizuuchi, K., and Funnell, B.E. (2012). Surfing biological surfaces: exploiting
791 the nucleoid for partition and transport in bacteria. Mol Microbiol *86*, 513-523.

792 Vecchiarelli, A.G., Neuman, K.C., and Mizuuchi, K. (2014). A propagating ATPase gradient
793 drives transport of surface-confined cellular cargo. Proc Natl Acad Sci U S A *111,* 4880-4885.

794 Watanabe, E., Wachi, M., Yamasaki, M., and Nagai, K. (1992). ATPase activity of SopA, a protein
795 essential for active partitioning of F plasmid. Molecular & general genetics : MGG *234*, 346-352.

796 Yamaichi, Y., and Niki, H. (2000). Active segregation by the Bacillus subtilis partitioning system
797 in Escherichia coli. Proc Natl Acad Sci U S A *97*, 14656-14661.

Figure Supplements:

Figure 2—figure supplement 1 *and legend*.

Figure 2—figure supplement 2 *and legend*.

Figure 2—figure supplement 3 *and legend*.

Figure 4—figure supplement 1 *and legend*.

Figure 5—figure supplement 1 *and legend*.

Figure 6—figure supplement 1 *and legend*.

Figure 6—figure supplement 2 *and legend*.

Figure 6—figure supplement 3 *and legend*.

808 Figure 2—figure supplement 1. *Gel filtration column elution profile of $ParB_F^{1-42}$-mCherry.*

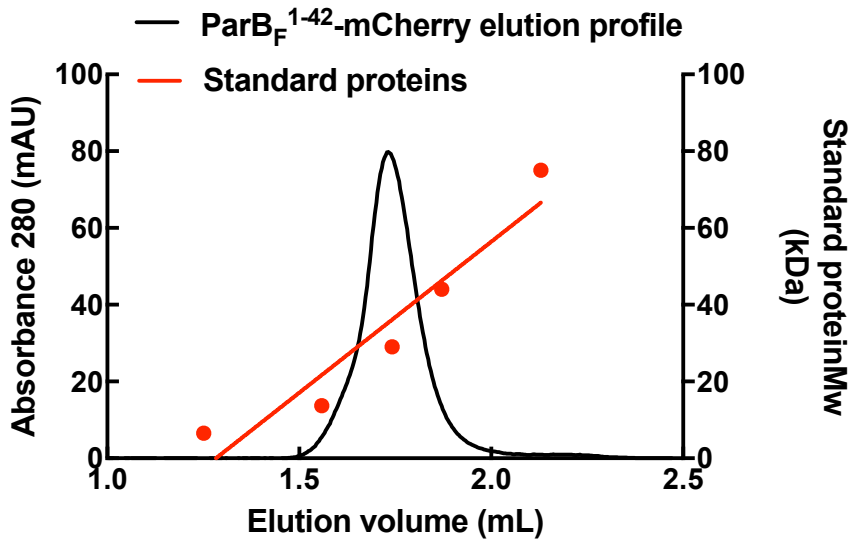

809

810 *Figure 2—figure supplement 1.* The elution profile of $ParB_F^{1-42}$-mCherry on a Superose 6 3.2/300 column (GE
811 Healthcare) with a standard curve generated using a protein standards kit (GE Healthcare). The molecular weight
812 of $ParB_F^{1-42}$-mCherry was estimated to be ~35 kDa, close to the predicted molecular weight for a monomer of
813 ~33 kDa.

814 Figure 2—figure supplement 2. FRAP of $ParA_F$-eGFP and $ParB_F^{1-42}$-mCherry on DNA-
815 carpet.

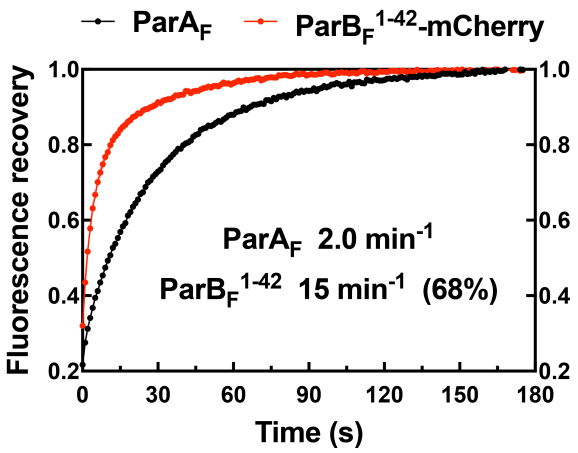

816

817 *Figure 2—figure supplement 2.* $ParB_F^{1-42}$-mCherry exchanged significantly faster than $ParA_F$ after photo-
818 bleaching. Data have been normalized to the maximum fluorescence recovery. The data were fitted to a single-
819 exponential curve for $ParA_F$ and a double-exponential curve for $ParB_F$, which did not fit a single-exponential
820 recovery curve. $ParA_F$ recovered with k_{excg} ~2.0 min^{-1}, and $ParB_F$ recovered with k_{excg} ~15 min^{-1} for the faster
821 (68%) and ~2.0 min^{-1} for the slower recovery components. Multi-exponential recovery kinetics can be explained
822 by the relatively large bleached area causing variable diffusion distance for the unbleached molecules need to
823 travel for full fluorescence recovery of the bleached area (this affects recovery of faster recovering components
824 more significantly). An alternative explanation that assumes presence of 30% population of stable $ParA_F$-$ParB_F^{1-}$
825 ^{42}-mCherry complex is unlikely since the buffer wash experiment (Figure 2D) did not support presence of such
826 species.

Figure 2—figure supplement 3. $ParA_F$ ATPase stimulation by $ParB_F^{1-42}$-mCherry-$EcoRI^{E111Q}$ is not influenced by the addition of DNA fragment containing EcoRI recognition sequence.

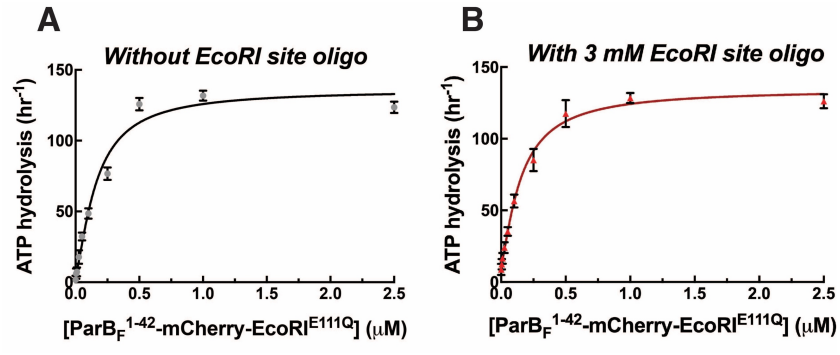

827 *Figure 2—figure supplement 3*. (A) $ParA_F$-ATPase activation curve of $ParB_F^{1-42}$-mCherry-$EcoRI^{E111Q}$ in the
828 absence of the EcoRI sequence duplex (Figure 2G) is shown for comparison. (B) $ParA_F$-ATPase activity was
829 measured in the presence of EcoRI-digested pBR322 DNA (60 μg/ml), 77 bp duplex DNA fragment containing
830 two EcoRI recognition sequences (5'-
831 ATTCTCTTGGGACCACGGTCCCAACTTGGATTCTCGGTCTGATAATCAGACTGGGACCACGGTCC
832 CACTCGGGATTC plus complement; 1.5 μM) and different concentrations of dimeric $ParB_F^{1-42}$-mCherry-
833 $EcoRI^{E111Q}$.

834

835 Figure 4—figure supplement 1. Determination of $ParB_F$ monomer-dimer Kd by FRET.

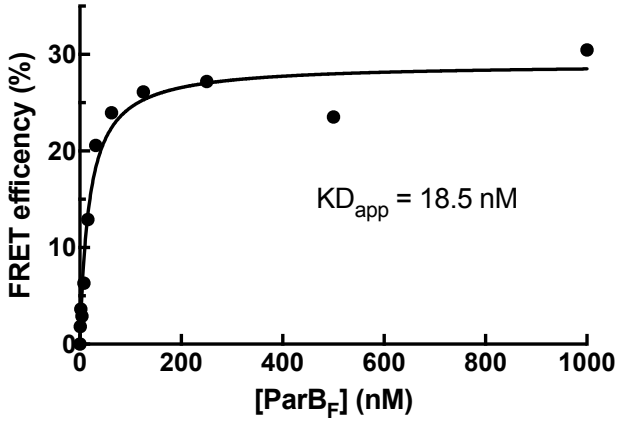

836

837 *Figure 4—figure supplement 1.* In order to estimate the Kd for dimerization of $ParB_F$ two batches of protein
838 were separately labeled with Alexa 488 or Alexa 564 then mixed at equal concentrations, the sum of which are
839 shown on the *x*-axis. The FRET efficiency was measured using a fluorescence plate reader (Clariostar Plus,
840 BMG Labtech). Assuming the observed FRET efficiency linearly correlates to the fraction of the protein in the
841 dimer state, the apparent Kd for dimerization of $ParB_F$ was estimated to be ~18.5 nM.

842

843 Figure 5—figure supplement 1. Binding curves for $ParA_F$ and either: $ParB_F$ with CDP or

844 $ParB_F$ with CTP associating with the DNA-carpet.

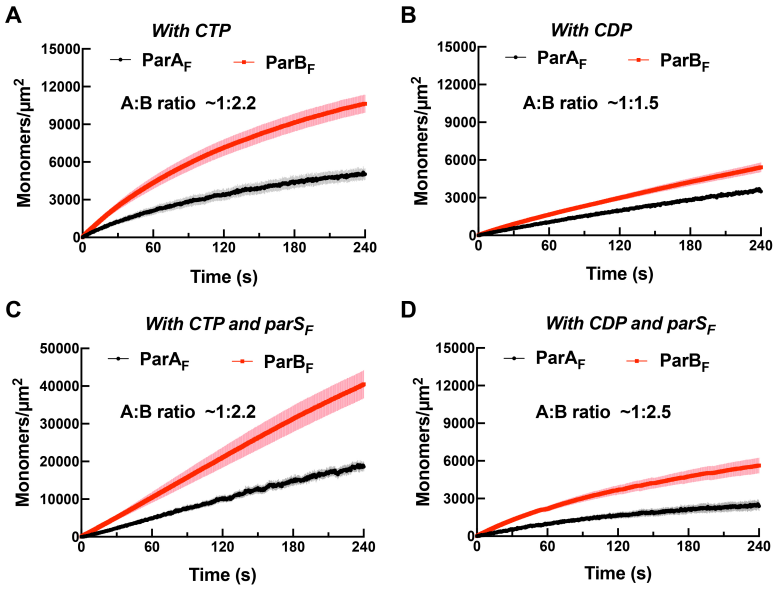

845

846 *Figure 5—figure supplement 1.* (A) $ParA_F$-eGFP (1 µM) and $ParB_F$-Alexa647 (2 µM) preincubated in the

847 presence of ATPγS and 2 mM CTP were infused into the nsDNA-carpeted flow cell. (B) $ParA_F$-eGFP (1 µM)

848 and $ParB_F$-Alexa647 (2 µM) preincubated in the presence of ATPγS and 2 mM CDP were infused into the

849 nsDNA-carpeted flow cell. (C) $ParA_F$-eGFP (1 µM) and $ParB_F$-Alexa647 (2 µM) preincubated in the presence

850 of 24bp $parS_F$ DNA fragment (1.1 µM), ATPγS and 2 mM CTP were infused into the nsDNA-carpeted flow cell.

851 (D) $ParA_F$-eGFP (1 µM) and $ParB_F$-Alexa647 (2 µM) preincubated in the presence of 24bp $parS_F$ DNA fragment

852 (1.1 µM), ATPγS and 2 mM CDP were infused into the nsDNA-carpeted flow cell.

853

854 Figure 6—figure supplement 1. *Stepwise de-condensation of condensed DNA tethers in the*
855 *presence of CDP or CTP by tensile force: condensation observed in the presence of CDP is*
856 *unstable*.

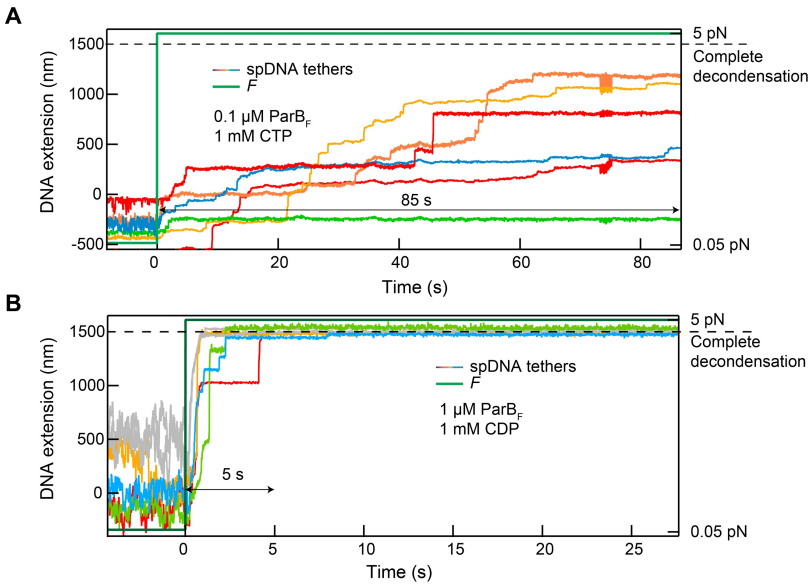

857

858 *Figure 6—figure supplement 1*. (A) The extension of 5 DNA tethers containing *parS$_F$* sequences (colored solid
859 lines, left y-axis) were simultaneously measured at a force (green solid line, right y-axis) of 0.05 pN after the
860 introduction of ParB$_F$ (0.1 μM) and CTP (1 mM). The tethers remained condensed for at least 85 s after the force
861 was increased to 5 pN. Most partial extension took place in discrete steps. (B) The same measurement as in (A)
862 except that the DNA was condensed with 10-fold more ParB$_F$ (1 μM) with CDP (1 mM). DNA condensation in
863 the presence of CDP was quickly reversed under high force (5 pN). After the force was increased to 5 pN (time
864 0) the extension of all five DNA tethers increased to their full decondensed length (dashed line) within ~5 s.

865

866

Figure 6—figure supplement 2. DNA tethers without $parS_F$ sequence are not condensed by $ParB_F$ and $parS_F$ in trans in the presence of CTP.

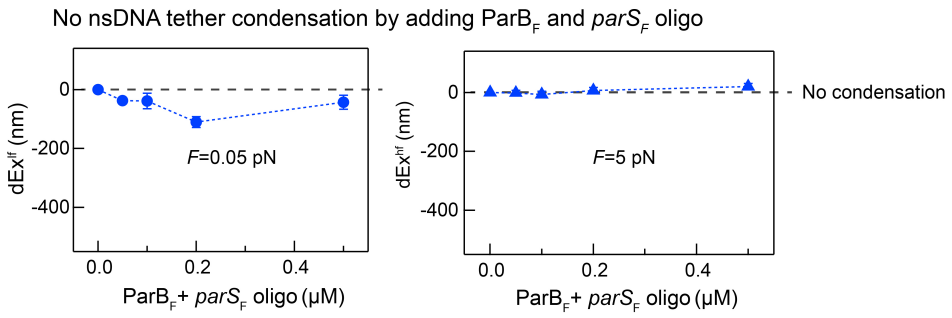

Figure 6—figure supplement 2. DNA tethers that did not contain a $parS_F$ site were not significantly condensed by the addition of $parS_F$ DNA fragment *in trans* with $ParB_F$ in the presence of CTP. The decreases in extension at 0.05 pN (blue circle, left panel) and 5 pN (blue triangle, right panel) are plotted as a function of the concentration of ParB and $parS_F$, which were added together at stoichiometric concentrations.

Figure 6—figure supplement 3. Mutation of a BoxII residue R121A does not affect the affinity of $ParB_F^{R121A}$ for $parS_F$, but neither the protein stoichiometry of the $ParA_F$-$ParB_F^{R121A}$ complex assembled on nsDNA prior to ATP hydrolysis, nor the extent of $ParA_F$-ATPase activation by $ParB_F^{R121A}$ is impacted by the presence of $parS_F$.

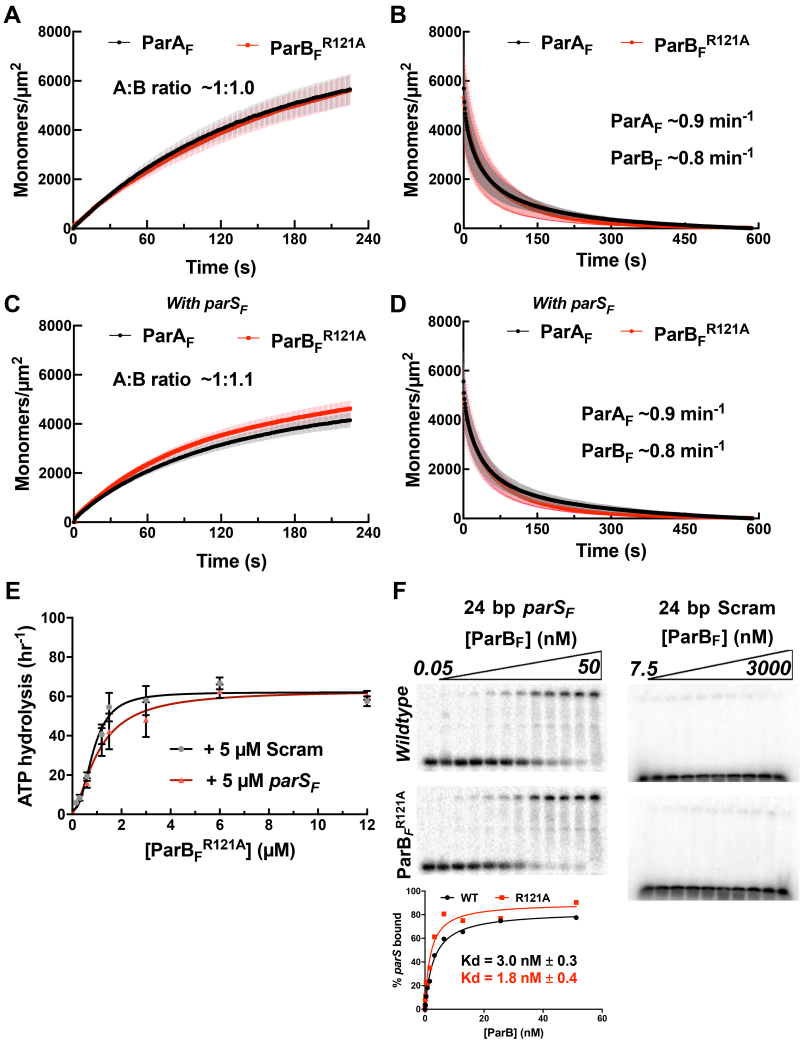

Figure 6—figure supplement 3. $ParA_F$ (1 µM) and $ParB_F^{R121A}$ (2 µM) were preincubated in the presence of ATPγS either without (A) or together with 24 bp $parS_F$ DNA fragment (1.1 µM, C), infused into to the DNA-carpeted flow cell and washed with buffer containing ATPγS (B, D). (E) $ParA_F$ ATPase activation by

$ParB_F^{R121A}$ was measured in the presence of EcoRI-digested pBR322 DNA (60 μg/ml) and different concentrations of $ParB_F^{R121A}$ either in the absence (black line) or presence (red line) of *parS*$_F$ (at 10% excess of the dimer concentrations of $ParB_F^{R121A}$). (F) The binding of $ParB_F$ or $ParB_F^{R121A}$ to 0.1 nM P^{32}-labeled 24 bp *parS*$_F$ DNA (left) or to 0.1 nM P^{32}-labeled 24 bp *scrambled* DNA (right) was measured by EMSA. The 4-12% gradient acrylamide gel was run in 1x TBE + 5 mM Mg_2Ac at 4 °C for 1 hour, 150 V. The gels were quantified (bottom) to estimate the *parS* binding Kd of $ParB_F$ and $ParB_F^{R121A}$.

873

Source Data Files (one Excel file with 19 sheets)

Figure 2-Source Data 1:

Numerical data for figure 2 panels A-E (Microsoft Excel).

Figure 2-Source Data 2:

Numerical data for figure 2 panels F, G (Microsoft Excel).

Figure 3-Source Data 1:

Numerical data for figure 3 panels A-C (Microsoft Excel).

Figure 3-Source Data 2:

Numerical data for figure 3 panels D (Microsoft Excel).

Figure 4-Source Data 1:

Numerical data for figure 4 panels A-D (Microsoft Excel).

Figure 4-Source Data 2:

Numerical data for figure 4 panels E (Microsoft Excel).

Figure 5-Source Data 1:

Numerical data for figure 5 panels A-E (Microsoft Excel).

Figure 5-Source Data 2:

Numerical data for figure 5 panels F, G (Microsoft Excel).

Figure 6-Source Data 1:

Numerical data for figure 6 panel A (Microsoft Excel).

Figure 6-Source Data 2:

Numerical data for figure 6 panel B-left (Microsoft Excel).

Figure 6-Source Data 3:

Numerical data for figure 6 panels B-right (Microsoft Excel).

Figure 6-Source Data 4:

Numerical data for figure 6 panels C (Microsoft Excel).

Figure 2-figure supplement 2-Source Data 1:

Numerical data for figure 2-figure supplement 2 (Microsoft Excel).

Figure 4-figure supplement 1-Source Data 1:

Numerical data for figure 4-figure supplement 1 (Microsoft Excel).

Figure 5-figure supplement 1-Source Data 1:

Numerical data for figure 5-figure supplement 1 (Microsoft Excel).

Figure 6-figure supplement 1-Source Data 1:

Numerical data for figure 6-figure supplement 1A (Microsoft Excel).

Figure 6-supplemental figure 1-Source Data 2:

Numerical data for figure 6-figure supplement 1B (Microsoft Excel).

Figure 6-supplemental figure 2-Source Data 1:

Numerical data for figure 6-figure supplement 2 (Microsoft Excel).

Figure 6-figure supplement 3-Source Data 1:

Numerical data for figure 6-figure supplement 3 panels A-D and F (Microsoft Excel).

918